MEMS Shear Sensor

Submitted By
Daniela Alejandra Torres

IN PARTIAL FULFILLMENT OF THE REQUIREMENTS FOR THE DEGREE OF

BACHELOR OF SCIENCE IN MECHANICAL ENGINEERING

School of Engineering
Tufts University
Medford, Massachusetts

May 2016

Signature of Author:
Daniela Alejandra Torres

Certified By:
Dr. Robert David White
Department of Mechanical Engineering
Tufts University

Committee:
Dr. Robert David White
Department of Mechanical Engineering
Tufts University

Committee:
Dr. Chris Rogers
Department of Mechanical Engineering
Tufts University

Abstract

A MEMS floating element shear stress sensor array has been fabricated at the Tufts Micro and Nano Fabrication Lab. Each device is designed to fit on a 1 cm^2 chip and consists of elements arranged in four different groups (A,B,C, and D). One group is orientated in the x direction, the other in the y direction, and two groups are oriented at a 45º angle to allow for sensing in both the x and y directions. This unique array layout is used to determine pressure gradient and shear stress sensitivity in two directions. Differential capacitance is measured using electrostatic sensing with a sense gap of 5 µm between a fixed electrode and floating element; these measurements lead to determination of shear stress.

The device is currently fabricated on a glass substrate using four layers using a surface micromachining process. Electrical interconnects are fabricated with 15 nm of Chromium and 150 nm of Gold evaporated or sputtered film. A seed layer consists of 30 nm of Titanium and 300 nm of Copper also evaporated or sputtered followed by a 5 µm thick Copper plated sacrificial layer. Finally, a 10 µm thick layer is Nickel plated to form the structure of the device. Much of the focus of this thesis is on improving this with particular emphasis on the quality and stress of these metal films.

Mechanical, electrostatic, and fluid modeling suggests that each device exhibits lower pressure gradient sensitivity and a higher shear stress sensitivity compared to the previous generation. Currently, modeling results have indicated that for groups A and C in the device pressure gradient sensitivity is -0.6 aF/ (Pa/mm), and shear stress sensitivity is 0.15 fF/Pa. In groups B and D pressure gradient sensitivity is expected to be -0.3 aF/

(Pa/mm), while shear stress sensitivity is 0.074 fF/Pa. It should be noted that low pressure gradient sensitivity is considered a desirable attribute for these sensors.

Most recent chips, gathered from wafers that have undergone the most recent and updated fabrication process, have at least two working capacitors; making them good candidates for flow testing in the near future. From these chips capacitance values for groups A and C are around 9-9.5 pF, and 4.5-5 pF for groups B and C; These are slightly higher values compared to modeling predictions (2 pF). Laser Doppler Vibrometry data suggests there exists a vertical bouncing mode frequency of 120 kHz and a pitch mode frequency of 66 kHz. These values are also higher than suggested from modeling results which suggested a bouncing mode frequency of 25.2 kHz and a pitch mode frequency of 19.5 kHz.

Acknowledgements

I would like to thank my advisor, Professor Robert White. Since the first days of ME 37 I've admired his clarity, thoughtfulness, and professionalism in his work. Because of him, I have learned an incredible amount through exciting and challenging research. I would like to thank him for all the times he spent answering any of my questions, or guiding me in the lab. I have concluded that MEMS is a topic I want to pursue further. Finally, I'd also like to thank Professor White for his kindness and sense of humor.

I would also like to thank Professor Chris Rogers who has served as my other committee mentor on this project. He has always made time to meet me and advise me on my academics. I would like to thank him for reviewing this thesis.

Next, I would like to thank everybody in Professor White's research group. Kevin, Niko, Peter, Grace, Ernest and Wang have all welcomed me with smiles and have always given time away from their own work to answer any questions of mine and give me graduate school advice. Kevin, Niko, and Wang have also been there to assist me in the lab with various fabrication processing. I'd like to thank Wang for going to Harvard CNS for depositing some material for us.

Additionally, I would like to thank Jim Vlahakis and other Micro Fab users, that I have met through various training sessions, from being in the clean room, and being at 200 Boston. I've enjoyed learning about other research going on at Tufts and being a part of the Tufts Micro and Nano Fabrication Lab community.

Finally, I would like to thank my parents, siblings, and boyfriend. Their love and support keeps me going, and they have always been there to listen and offer moral support.

Table of Contents

1 Introduction ... 1
1.1 Contributions ... 1
1.1.1 Element and Array Design ... 1
1.1.2 Quasistatic Models ... 2
1.1.3 Fabrication ... 2
2 Background ... 3
2.1 Indirect vs. Direct Shear Measurements ... 3
2.2 Examples of MEMS Shear Sensors ... 5
2.3 Shear Stress in MEMS ... 9
3 Design ... 11
3.1 Element Design ... 11
3.2 Array Design ... 13
3.3 Quasistatic Models ... 16
3.3.1 Mechanical Modeling ... 16
3.3.2 Electrostatic Modeling ... 22
3.3.3 Fluids Modeling ... 27
3.3.4 System Modeling ... 30
4 Fabrication ... 36
4.1 Chromium and Gold Metal Layer ... 37
4.2 Seed and Sacrificial Layers ... 39
4.3 Structural Nickel Layer and Release of Floating Elements ... 43
4.4 SEM Images ... 48
5 Changes to the Fabrication Process ... 51
5.1 Change of Process Thickness of Cr/Au Layers and Stress in Multilayered Films 51
5.2 Seed and Copper Layer ... 56
5.3 SiO_2 as a Passivation Layer ... 58
6 Experimental Results ... 59
6.1 Stress in Cr/Au Films ... 59
6.2 Thick Ti/Cu Sputtering ... 60
6.3 Cr/Au and Ti/Cu Evaporation at Harvard CNS ... 64
6.4 Results from RF SiO_2 Sputter ... 72
7 Conclusion and Future Work ... 74
7.1 Hardware ... 74
7.2 Modeling ... 75
7.3 Future Work ... 76
7.3.1 Fabrication ... 76
References ... 79
Appendix A Alignment Slide Mask ... 80
Appendix B Surface Micromachining Runsheet ... 80

Table of Figures

Figure 2-1 Fringe patterns observed in oil film after oil is thinned due to shear 4
Figure 2-2 Element design and image of key fabrication steps 6
Figure 2-3 (a) Schematic of MEMS floating element shear sensor taken from [1]........... 7
Figure 2-4 Fabrication process of MEMS shear sensor taken from [1]. 8
Figure 2-5 SEM image of MEMS shear sensor taken from [2] 9
Figure 3-1 Element layout of shear sensor. 11
Figure 3-2 Displacement of floating element in response to shear. 12
Figure 3-3 Array layout of shear sensor device 14
Figure 3-4 Mesh for solid mechanics model of shear sensor... 16
Figure 3-5 Modal analysis of shear sensor in vacuo 18
Figure 3-6 Static response of MEMS shear sensor in COMSOL 20
Figure 3-7 Static response of MEMS shear sensor in COMSOL 21
Figure 3-8 2D linear electromechanical study made in COMSOL. 23
Figure 3-9 2D linear electromechanical study made in COMSOL. 23
Figure 3-10 Change in capacitance for one side of one element (fF) vs. lateral deflection of the shuttle (μm).. 25
Figure 3-11 Change in capacitance for one side of one element (fF) vs. vertical deflection of the shuttle (μm).. 26
Figure 3-12 Change in capacitance for one side of one element (fF) vs. pitching rotation of the shuttle (deg) 27
Figure 4-1 Overview of the surface micromachining process 36
Figure 4-2 MEMS shear sensor interconnects necessary for capacitance measurements 39
Figure 4-3 Close up of shear stress sensor after the second lithography 40
Figure 4-4 Final Ti/Cu 30/300 nm sputtered seed layer after liftoff................................ 42
Figure 4-5 MEMS shear sensor post Ni plating... 45
Figure 4-6 Image of MEMS shear sensor at the end of the surface micromachining process.. 47
Figure 4-7 A close up image near the anchor region 47
Figure 4-8 A close up image of the sense gap. 48
Figure 4-9 SEM image of shear sensor with cut outs 49
Figure 4-10 SEM image of beam width (6.92 μm) and beam gap width (2.55 μm). 49
Figure 4-11 SEM image of sense gap width (3.54 μm).. 50
Figure 5-1 Image of film defects on Cr/Au (75/225 nm) after sputtering at 5 mT. 52
Figure 5-2 Image of Cr/Au blister caused by compressive stress.................................... 53
Figure 5-3 Top view of the alignment configuration for curvature measurements 55
Figure 5-4 Failed Cu plated layer. 57
Figure 6-1 Center of Slide Stress (GPa) vs. Process Pressure of Cr/Au film 59
Figure 6-2 50 nm/ 4 μm of sputtered Ti/Cu in the NSC3000 sputter tool. 60
Figure 6-3 Residue observed around the edges 61
Figure 6-4 Grainy residue observed underneath Nickel film... 63
Figure 6-5 SEM image released elements that underwent thick Ti/Cu sputtering 63
Figure 6-6 New observed failure mode 64
Figure 6-7 Image of MEMS shear sensor wafer after Cr/Au (15 nm / 150 nm) Evaporation from Harvard CNS. 66

Figure 6-8 Image of MEMS shear sensor wafer after Ti/Cu (30 nm / 300 nm) evaporation from Harvard CNS. 66
Figure 6-9 SEM image of two shear sensor elements that have undergone Cr/Au and Ti/Cu evaporation at Harvard CNS 68
Figure 6-10 Close up SEM image of a MEMS floating element from the same chip 69
Figure 6-11 Close up SEM image of MEMS shear sensor from the same chip 69
Figure 6-12 LDV data on chip 19. 71
Figure 6-13 Image of MEMS shear sensor wafer after RF SiO_2 Sputtering. 72
Figure 6-14 Cracking observed in RF sputtered SiO_2 73
Figure 7-1 Patterned electroless plated Nickel on patterned plated Copper. 76

Table of Tables

Table 3-1 Material and Mesh Properties for model 17
Table 3-2 Summary of stiffness results (given model and analytical estimates), beam geometry values, force, displacement (tilt, lateral, and vertical) from COMSOL model. 20
Table 3-3 Summary of Results for 2D Linear Analysis of Static Capacitance Values of MEMS Shear Sensors 24
Table 3-4 Change in Capacitance for modeled side of element in COMSOL. Linear fit data based on figures 3.10, 3.11, and 3.12. 27
Table 3-5 Fluids Model Parameters and Force Results 29
Table 3-6 Summary of Total Expected Sensitivity in all Groups of Shear Sensor Device 32
Table 3-7 Motion and sensitivity due to shear and a pressure gradient in flow and pitch directions given 2D laminar poiessuille flow. 34
Table 3-8 Total Sensitivity due to shear, total sensitivity each group of the MEMS shear sensor from a combination of fluids, electrostatic and structural model. 34
Table 3-9 Pressure gradient and shear stress sensitivities for all groups of current design and previously determined shear stress and pressure gradient sensitivity from the [2].... 35
Table 5-1: Properties Microscope Soda Lime Glass Slides 54
Table 5-2 Dektak Scan Parameters for Curvature and Stress Measurements 56
Table 5-3 Material Properties of <100> Silicon Wafer 56
Table 6-1 Resistance and Capacitance data on released MEMS Shear Sensors. These sensors underwent a thick 5 µm sputtered copper deposition. Most elements exhibited low resistance values indicating that the floating element is stuck down. More data on other chips can be seen in Appendix 3 62
Table 6-2 Resistance and Capacitance data on released MEMS Shear Sensors. These sensors underwent Cr/Au and Ti/Cu evaporation, 5 µm plated Ti/Cu sacrificial layer, >1 week etch, and CPD drying. Many groups experienced high resistance leading to the conclusion that these elements aren’t stuck down. 67

1 Introduction

Wall shear can be used to understand boundary layer transition, separation, and drag at a surface [1]. Drag is of particular interest in the aero sciences for the development of light structures and improving these structures to lower fuel consumption. Currently, most methods implemented to measure shear stress (i.e oil film interferometry) are difficult to do during flight, are time consuming, or require complex calibration since they are not direct measurements [1]. MEMS shear stress sensors are a useful alternative method to shear stress measurements. Advantages include their capability to measure shear stress directly, while also not disrupting airflow [1].

When determining shear stress in laminar or turbulent flow regimes a MEMS shear sensor may exhibit two types of sensitivities. The first is a sensitivity due to shear stress, the desired parameter, which leads to direct shear stress measurements as the sensor undergoes flow during performance. The second is a sensitivity due to a pressure gradient which must also be determined in order to remove pressure gradient effects from the measurement. It was found in previous tests that pressure gradient effects have a substantial impact on total sensitivity [2]. The focus of this thesis will be on a new generation of shear sensors fabricated at the Tufts Micro and Nano Fabrication lab that are designed to decrease the effects of a pressure gradient and increase the sensitivity due to shear.

1.1 *Contributions*

This section of the thesis will focus on personal contributions to the project done in the last year; which highlight important aspects of this thesis.

1.1.1 Element and Array Design

A unique array layout in a 1 cm^2 chip consisting of four different groups will allow for calculating shear stress and pressure gradient effects in two directions. A new element design includes less surface topology, and for some elements, modifications to element geometry to provide linearly independent responses to shear and pressure

gradient. Most of this thesis work has been to understand this new design, make comparisons to the older design, and understand how to distinguish between both pressure gradient and shear stress measurements.

1.1.2 Quasistatic Models

Mechanical, electrostatic, and fluid modeling are essential for gaining insight into device performance, and create qualitative predictions of performance to compare to actual measurements during device testing. The contribution here has been to break apart these models and understand how information gathered from each separate model come together to form predictions on shear stress and pressure gradient sensitivity.

1.1.3 Fabrication

Surface micromachining has been the largest challenge for this project. Most of the thesis work here has been to extensively explore each aspect of the process and optimize for high quality and low stress films. Much of this has caused changes to the original process. Key changes have included changes in Cr/Au layers, which originally stemmed from stress studies in Cr/Au films, changes to how Ti/Cu is deposited after observing that this was one of the most contaminated films, and finally the exploration of other possible methods to limit stiction such as the deposition of SiO_2 in a new sputter tool that has encountered little to no contamination.

2 Background

In this chapter differences between indirect and direct shear stress measurements will be highlighted, and three different floating element shear stress sensors found in literature will be introduced to give insight on this technology. Focus will be spent on design and fabrication of these shear sensors. One of the three shear sensors discussed is the previous generation of the Tufts shear sensor; throughout the thesis this older generation of shear sensors will be referenced since its fabrication methods parallel the methods discussed in the upcoming chapters. A brief description of how shear force relates to the displacement and stiffness of a MEMS floating element will also be presented in this chapter.

2.1 Indirect vs. Direct Shear Measurements

Indirect measurements typically involve a set of assumptions used to determine a quality of interest, and requires one to produce a model to estimate the quality of interest from the measured quality. Direct measurements attempt to directly measure the quality of interest. In the case of shear stress measurements both indirect and direct methods are used.

One method of indirect shear stress measurement is oil film interferometry, which relates the rate of oil film thinning on a surface, when exposed to flow, to shear stress. Oil thinning is also affected by gravity, pressure gradients, surface tension of the oil, and curvature of the oil [3]. After oil undergoes thinning due to shear, constructive and destructive patterns along a surface are observed, indicating thickness change in the oil. Spacing between these fringe patterns in the film are proportional to skin friction [3]. Some essential components to oil film interferometry are: a light source, and detector (i.e a camera). An image of oil film thinning after undergoing shear can be seen in figure 2.1.

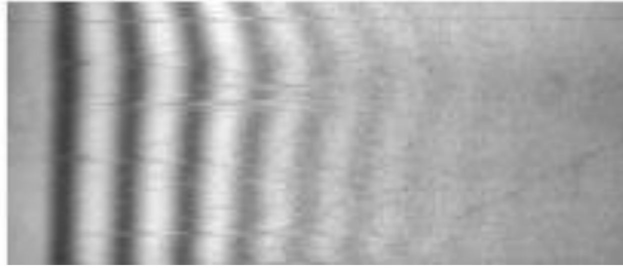

Figure 2-1 Fringe patterns observed in oil film after oil is thinned due to shear. Image taken from [3].

Some advantages of oil film interferometry include the ability to measure shear stress in two or three dimensions, ability to be applied to curved surfaces, and the ability to make measurements with high resolution. Some disadvantages include the need for high reflective surfaces, lengthy setup, testing, and data collecting times, the need for governing assumptions (i.e assumptions about environmental temperature, properties of oil, fluid flow etc), and challenges with in flight testing implementation [3].

A method of direct shear stress measurement is through MEMS floating elements. Floating elements involve a shuttle that is located above a surface and suspended with beams. As this shuttle experiences forces due to flow it deflects, and the beams create a restoring force on the shuttle which allows the device to be modeled as a spring-force system. Careful design of beam geometry, and gap width allow the sensor to behave linearly. The deflection of the shuttle may be detected by measuring capacitance changes (differential capacitance measurements), with piezo resistance sensors or optical methods. The two most recent shear sensor devices implemented at the Tufts Micro and Nano Fabrication Lab use MEMS floating elements and implement differential capacitance measurements.

Some advantages of MEMS floating elements are: ease of use (compared to oil film interferometry), high resolution, quicker measurement implementation, direct measurement (eliminate the use of many assumptions), and the ability to avoid disrupting fluid flow due to its small size. Some disadvantages include sensitivity to pressure gradient and environmental effects, potentially weak robustness to environmental effects, and challenges associated with mounting the sensors, particularly onto curved surfaces.

2.2 Examples of MEMS Shear Sensors

The MEMS shear sensors discussed here implement floating elements and differential capacitance measurements. Key differences between all three sensors involve different fabrication decisions and element design. The first design is that of Martin Schmidt, Roger Howe, Stephen Senturia, and Joseph Haritonidis, and is considered one of the earliest MEMS floating element shear sensor designs.

Fabrication of this sensor begins with a Silicon wafer that contains PMOS transistors. A CVD SiO_2 layer is deposited to form a passivation layer to protect these transistors throughout fabrication. A polyimide layer is deposited to protect the SiO_2 from experiencing cracking during the deposition of Aluminum, which is used as a sacrificial layer for this device. After evaporating a 3000 Å thick Aluminum sacrificial layer more polyimide is spun to form the structure of the floating element. Polyimide was chosen for this device since as it is spun on the surface a planarized layer is formed which is attractive in shear sensor applications since topology may cause disturbances while undergoing flow [4]. Polyimide has also been found to be under tensile residual stress after deposition which is desired in a floating element to keep the element suspended above a surface and provide a restoring force as it deflects [4].

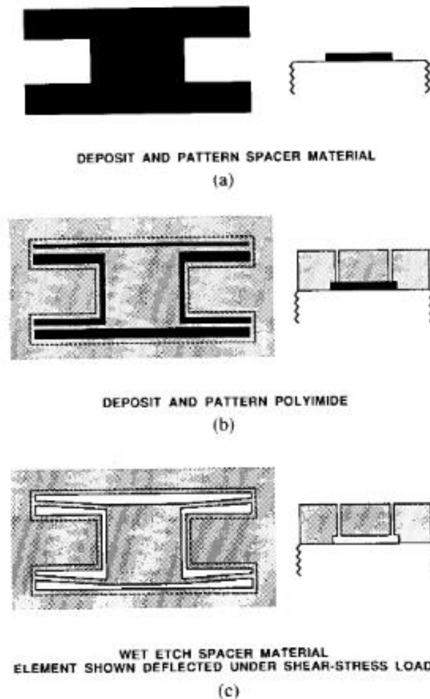

Figure 2-2 Element design and image of key fabrication steps taken from [4]. Here the spacer material is evaporated Aluminum, and in c. Aluminum undergoes a wet etch to release structures.

The element consists of four beam tethers that are used to suspend the shuttle. An image of the element design, and a cross section of its critical fabrication steps can be seen in figure 2.2. During fabrication it was found that using an evaporated Chromium layer to form thin conductors, on the surface of the wafer and underneath the floating element, worked better than evaporated Aluminum since high compressive stresses in Aluminum formed buckled conductors with some topology. The tensile nature of evaporated Chromium was found to create flatter conductors [4]. These conductors are critical for this device since this device senses deflections of the shuttle via differential capacitance measurements. This device is capable of responding to shear stress up to 12 Pa in laminar flow [4].

A second MEMS shear sensor floating element design is that of Tao Pan, Daniel Hyman, Mehran Mehregany, Eli Reshotko, and Steven Garverick. A first generation model of this device utilizes four beam tethers on either side of the floating element, as well as comb fingers for differential capacitance sensing [1]. This device was capable of measuring laminar shear up to 5 Pa [1]. An image of the sensor design, and an SEM image of the actual sensor can be seen in figure 2.3.

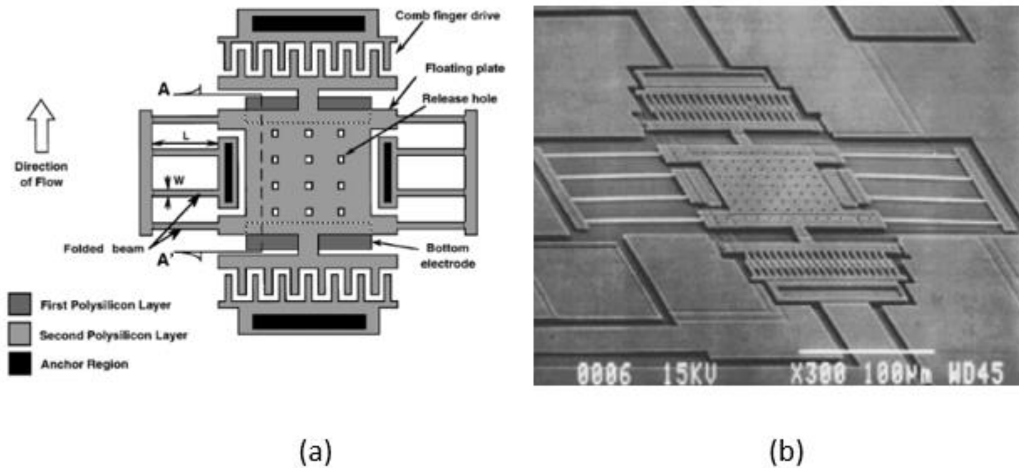

(a) (b)

Figure 2-3 (a) Schematic of MEMS floating element shear sensor taken from [1]. Four beam theters on either side of the floating plate are used to suspend the structure. Comb fingers are used to sense deflection of the shuttle. Various anchors are used throughout the device for support and release holes consists of bumps underneath the shuttle used to avoid stiction during release. (b) SEM image of a released element taken from [1].

Fabrication begins on a Silicon wafer with a thermally grown SiO_2 that is used to relieve stress between the substrate and the following Silicon Nitride layer. Silicon Nitride is used to insulate the shear sensor device from the Silicon wafer. Electrodes are formed using doped Polysilicon, and a sacrificial layer is made of SiO_2. The sacrificial layer consists of small grooves that will be used to form bumps underneath the main structural layer (floating element). The floating element is also made of Polysilicon and is released when the sacrificial layer is removed in an HF etch. The bumps underneath the shuttle allows for the structure to avoid stiction during release. An image of the fabrication process can be seen in figure 2.4.

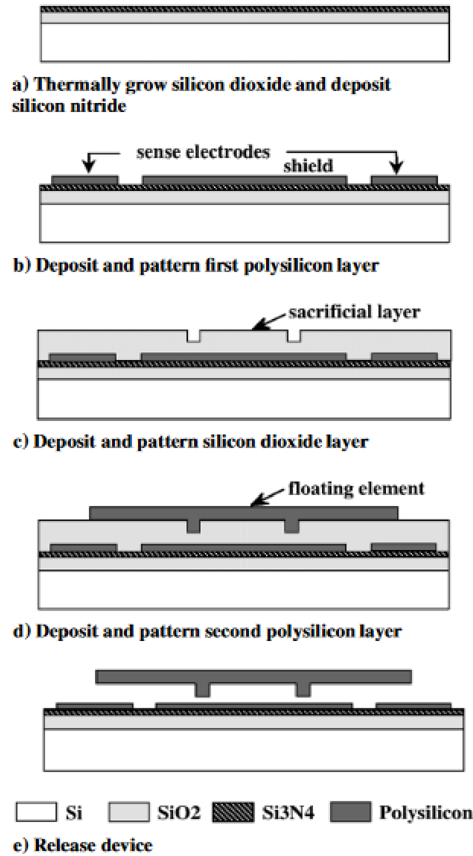

Figure 2-4 Fabrication process of MEMS shear sensor taken from [1].

A third MEMS shear sensor device is the design by Zhengxin Zhao and Robert White. This device is the previous generation of shear sensors from the shear sensors researched in this paper. The device consists of 8 beam tethers integrated within the area of the center shuttle. The device follows that of Pan's in that is uses comb fingers to sense capacitance changes as the shuttle deflects. Anchor regions and bumps on the surface of the shuttle also exist; these bumps were used in hopes of increasing the device's sensitivity to shear by allowing fluid flow to make more direct contact with the elements surface, however, it was later found that increased topology caused more sensitivity to a pressure gradient as it potentially allowed for a fluid to flow in a complicated manner around these surfaces. An image of the device can be seen in figure 2.5.

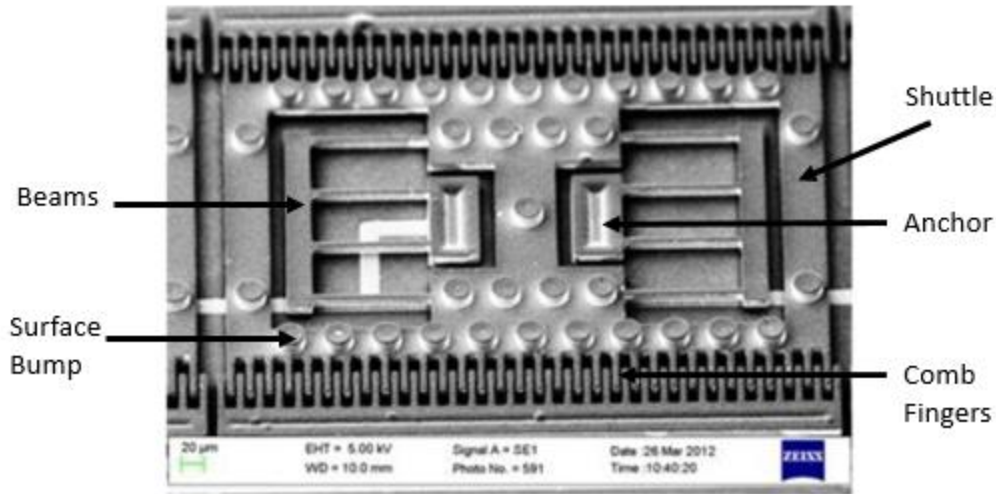

Figure 2-5 SEM image of MEMS shear sensor taken from [2]. In this design beams are incorporated within the area of the central shuttle and comb fingers are used for differential capacitance sensing. Anchors and surface bumps also exist. Anchors are used to support the suspended structure, and bumps were used in hopes of increasing the device's sensitivity to shear.

Fabrication of this device follows a similar surface micromachining process that is described in this thesis with some key changes described in later chapters. Other changes include the removal of surface bumps, different beam design, different array design and the removal of comb fingers in the generation of shear sensors described in this paper. Zhengxin's shear sensor design was capable of measuring laminar shear greater than 13 Pa.

2.3 Shear Stress in MEMS

An object exposed to flow experiences surface shear since the viscosity of the fluid (μ) applies a force on that objects surface. By assuming the fluid is Newtonian, which is applicable to a fluid like air, shear stress (τ_w) can be related to a fluid's flow velocity profile ($\frac{\partial u}{\partial y}$) by the relationship shown in equation (1) [1].

$$\tau_w = (\mu \frac{\partial u}{\partial y})_{y=0} \qquad (1)$$

In MEMS floating elements the beams suspending the shuttle react to the shear force from the flowing fluid by applying a restoring force; acting like springs in this system. The displacement of the shuttle (δ) is therefore directly related to shear stress (τ_w) by the relationship shown in equation (2) [1]. The stiffness, k, is determined by the material properties and geometry of the beams suspending the shuttle, and the area, A, represents the area of the device that undergoes shear. Deflection of the device is measured using differential capacitance methods.

$$k\delta = A\tau_w \tag{2}$$

This model gives the essential idea of the response of a floating element, but is overly simplistic as it ignores pressure gradient, pitching moment from aerodynamic forces, and three dimensional motion of the shuttle. These additional forces will be captured in the Design section of this thesis via COMSOL modeling results, and will also be captured in flow testing of these devices in the future.

3 Design

The first section in this chapter describes the design of an individual shear sensor element. Important characteristics and parts of the element are highlighted. In the second section the array design of an individual MEMS shear sensor chip is described. In the third section mechanical models, electrostatic models, and fluid models are described in order to make predictions of how this sensor may behave during operation.

3.1 Element Design

The design layout for each shear sensor element can be seen in figure 3-1. The size of each element is 400 µm x 510 µm. Each element consists of a 10 µm thick floating element, two fixed electrodes for differential capacitance sensing, folded beams, and anchors.

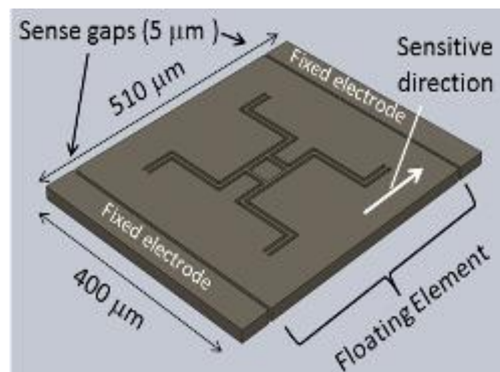

Figure 3-1 Element layout of shear sensor.

The floating element is suspended and anchored down at the center. The floating element experiences forces due to flow. This floating element includes folded beams that act as support and allow for spring behavior in the structure. The beam dimensions determine the overall stiffness of the structure. This is necessary for shear stress measurements (see sections 1.1, 1.2, 2.2.1). The beams are shaped in a crab leg structure to allow for reduced residual stress during fabrication release [2] a critical stage in the surface micromachining process.

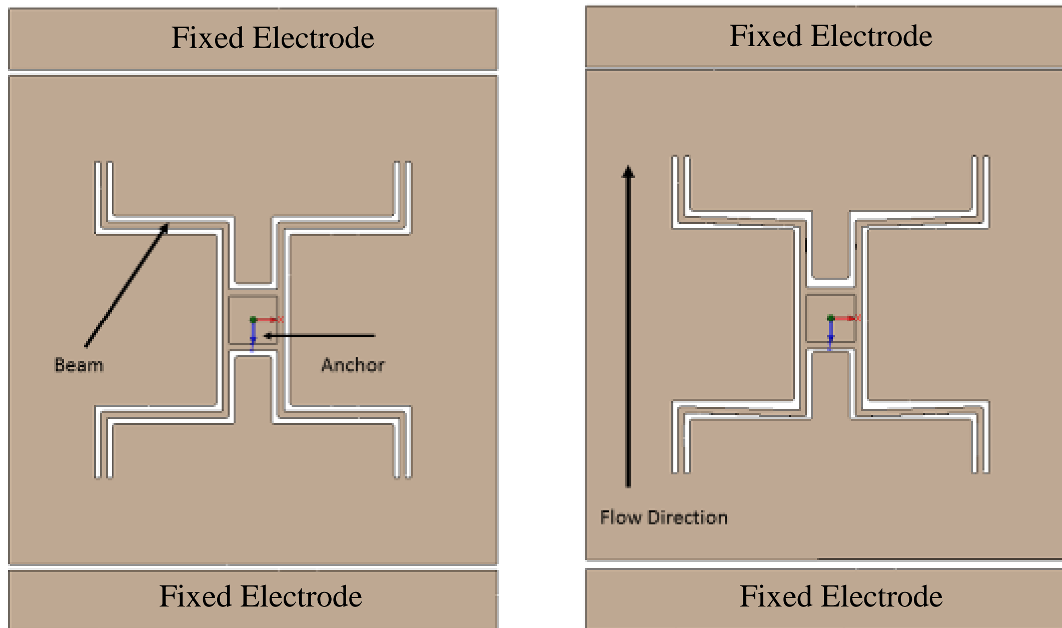

Figure 3-2 Displacement of floating element in response to shear. The image on the left shows the element prior to being exposed to any flow, and the image on the right shows the element displacing closer to the top electrode due to flow. Due to the anchor region the beams within the element experience some deflection.

Electrode walls and 5 µm gaps are introduced at two ends of the device in order to sense the floating element's motion. In this design comb fingers, from a previous design [2], were replaced with parallel electrodes to simplify some fabrication features. Despite this change the electrodes still serve its original purpose. As the floating element responds to a force due to flow the element displaces (See figure 3-2) causing one end of the floating element to approach closer to one of the fixed electrodes, while the other end displaces farther away from the other fixed electrode. At the end where the floating element nears the fixed electrode capacitance increases, while at the other end capacitance decreases. By measuring capacitance at both of the fixed electrodes and the floating element it is possible to determine the change in capacitance that occurs. These measurements are also necessary for shear stress measurements (see chapter 2).

Another change in this element design compared to previous versions of this shear sensor include the removal of surface bumps. These bumps were originally placed on the surface of the floating element in hopes of increasing sensitivity due to shear stress, however, it was found that it may have had a higher influence on the sensitivity due to a

pressure gradient instead [2]. This type of sensitivity is undesirable, thus in this new design focus has been spent on decreasing it as well as measuring it by introducing a special array layout (see section 3.2). Further details on this element and its impact in mechanical, electrostatic, and fluid models are discussed in later chapters where only quasistatic behavior of the element is studied.

3.2 Array Design

After testing previous versions of this shear sensor in a laminar flow cell, it was discovered that sensitivity due to a pressure gradient cannot be ignored [2]. Doing so will cause substantial errors in calculating shear stress sensitivity [2]. As a result it is important to include both sensitivities while calculating changes in capacitance. The relationship between changes in capacitance (ΔC) to shear stress sensitivity (S_2), single axis shear stress (τ_x), pressure gradient sensitivity (S_3), and a single axis pressure gradient ($\frac{\partial P}{\partial x}$) can be seen in equation (1) where the pressure gradient in this case is taken to be in the x direction [2].

$$\Delta C = S_2 \tau_x + S_3 \frac{\partial P}{\partial x} \quad (1)$$

Since there are two independent shear stresses (τ_x and τ_y) and two pressure gradients ($\frac{\partial P}{\partial x}$ and $\frac{\partial P}{\partial y}$) at a minimum four independent groups are required for full surface stress characterizations. Thus, there are now four independent groups of elements, labeled: A, B, C, D, oriented in different directions, as seen in figure 3-3, which differs from the original device that contained 16 identical groups [2].

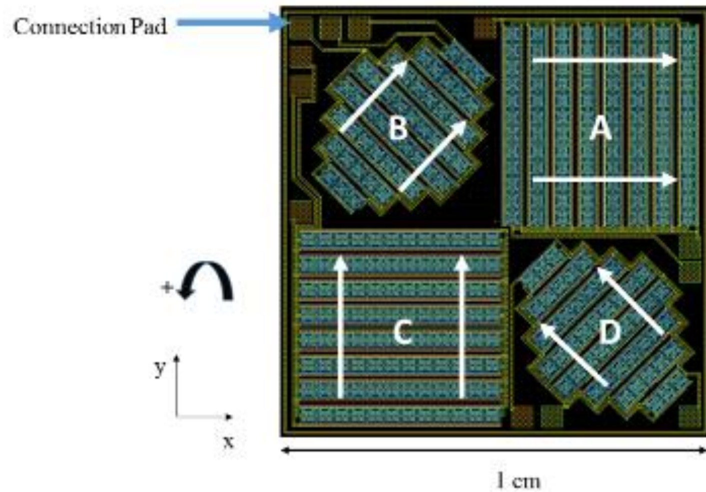

Figure 3-3 Array layout of shear sensor device. Given a coordinate axis elements in A are orientated in the x direction, elements in C are orientated in the y direction, and elements in B and D are orientated both in the x and y directions. The counterclockwise direction is chosen as positive with respect to this coordinate axis. Group B is oriented +45º with respect to the x axis and group D is oriented -45º with respect to the x axis

With this layout changes in capacitance in two directions due to shear stress and a pressure gradient may be measured. Groups A and C each contain 96 elements that are orientated in the x and y directions respectively. Groups B and D each contain 48 elements that are offset ±45º with respect to the x axis, allowing both groups to have components in the x and y directions. In addition to this offset, half of the chips on the wafer include cut outs in each floating element of groups B and D. This is done so that elements in groups B and D will experience a higher pressure gradient sensitivity than the elements in groups A and C. Images of these cutouts can be seen in section 3.6 where SEM images of these sensors after fabrication are discussed.

Rows of elements are connected in parallel in order to form each group, and each group takes up an area of about 25 mm^2. For differential capacitance measurement to be possible each group is connected to three electrical pads that serve as the route to the fixed electrodes on either side of the floating element, as well as the floating elements themselves. In this design, shear stress may be measured in a number of ways. Individual groups may be measured, groups may be measured in various combinations with each other, or the entire chip may be measured to determine the average shear stress over the entire MEMS chip.

As in previous designs this allows for a tradeoff between spatial resolution and sensitivity, and allows for continued functionality of the MEMS chip even if one to three of the groups is damaged during use or fabrication [2]. As mentioned in Zhengxin's work this may be important since shear sensors face harsh environmental conditions [2]. This has also been helpful during stiction tests after fabrication. Being able to measure each group individually has allowed for the search of working groups in chips where stiction is a concern, as well as determine in what ways the elements may be stuck down.

$$\begin{pmatrix} \triangle C_A \\ \triangle C_B \\ \triangle C_C \\ \triangle C_D \end{pmatrix} = \begin{bmatrix} S & 0 & P & 0 \\ \frac{S\sqrt{2}}{4} & \frac{S\sqrt{2}}{4} & \beta\frac{P\sqrt{2}}{4} & \beta\frac{P\sqrt{2}}{4} \\ 0 & S & 0 & P \\ \frac{-S\sqrt{2}}{4} & \frac{S\sqrt{2}}{4} & -\beta\frac{P\sqrt{2}}{4} & \beta\frac{P\sqrt{2}}{4} \end{bmatrix} \begin{pmatrix} \tau_x \\ \tau_y \\ \frac{\partial P}{\partial x} \\ \frac{\partial P}{\partial y} \end{pmatrix} \tag{2}$$

A matrix representation of how differential capacitance measurements (ΔC) are calculated in this MEMS shear sensor chip is shown in equation(2). S represents the sensitivity due to shear stress while P represents the sensitivity due to a pressure gradient. τ_x and τ_y represent shear stress in the x and y directions. $\frac{\partial P}{\partial x}$ and $\frac{\partial P}{\partial y}$ represent the pressure gradients in the x and y directions. Since groups B and D are oriented at a 45º offset, and have half the number of elements compared to groups A and C, S and P are multiplied by a factor of $\frac{\sqrt{2}}{4}$ in their respective sections of the matrix. By introducing cut outs to half of the chips on the wafer in the elements in groups B and D, P is further multiplied by a factor of β, which represents the increase in pressure gradient sensitivity. Introducing these cut outs and orientating B in the clockwise direction, and D in the counterclockwise directions allows this matrix to be invertible; thus solvable. If the pressure gradient and shear sensitivity were the same for all elements, β=1, the matrix would be singular and we would not be able to invert and determine the pressure gradient and shear from the measured capacitance change. Having this feature where half of the chips on the wafer include elements with cut outs will allow for further experiments to prove that the cut outs are useful for singling out pressure gradient measurements.

3.3 Quasistatic Models

This chapter explores mechanical, electrostatic, and fluid models of this MEMS shear sensor design. These models are used to predict both sensitivity (due to shear and a pressure gradient) and bandwidth performance of the sensor. These models provide insight into how the sensor may perform during calibration and testing. In all modeling only the steady response of the device is taken into account. All models were done in COMSOL.

3.3.1 Mechanical Modeling

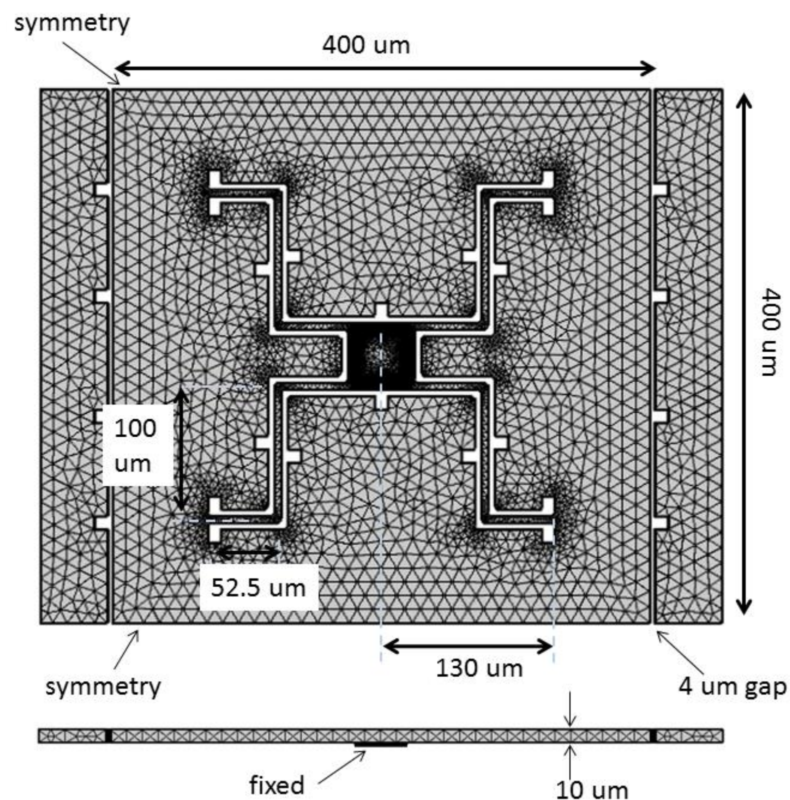

Figure 3-4 Mesh for solid mechanics model of shear sensor. Width of the floating element and electrode wall length are specified as well as important beam lengths of the crab leg structure and electrode gap length. Models were done with the middle anchor fixed underneath the 10 µm thick element. Thinnest structures include at least 3 mesh elements across.

A 2D model of the shear sensor was imported into COMSOL and extruded into a 10 µm thick three dimensional structure. Linear three dimensional solid mechanics analysis was used. An Eigen-frequency study was used to study the various vibrational modes of the structure, while two stationary studies were used to gain insight on vertical and lateral displacement of the shuttle. This information is useful for determining stiffness of the structure. For this Nickel structure a young's modulus (E) of 205 GPa [5], poisson's ratio (υ) of 0.31 [6], and density (ρ) of 2.9 g/cc was used. A fixed constraint is applied to the bottom of the element on the surface of the center anchor. A slide boundary condition is used at the ends of the element where it joins the next element in the group. The model is meshed using tetrahedral quadratic elements; including along the thickness of the structure. Mesh density is increased at corners where stress concentrations exist. These applications are necessary for accurate displacement and bending of the element.

The mesh can be seen in figure 3.4, and a summary of important properties of the COMSOL model can be seen in table 3.1. When modeling thin structures it is important to have enough mesh elements in the thinner parts of the structure. The smallest features on the shear sensor include the thickness and beam width of the shuttle. There are at least 3 elements across each of these features. For displacement studies this will play an important role to accurately modeling performance of the device.

Table 3-1 Material and Mesh Properties for model

Young's Modulus	219	Gpa
Poisson's Ratio	0.31	
Density	2.9	g/cc
Min Number of Mesh Elements	3	

The Eigen frequency model identifies the first four modes: a pitching mode about an axis through the anchor, a vertical mode out of plane of the structure, a lateral mode with a direction towards either electrode wall, and a sideways translational mode. Results of each mode can be seen in figure 3.5. Each mode has an impact on differential capacitance measurements since the distance between the floating element and electrode wall is sensed and determines displacement of the shuttle. In this study the element is

assumed to be in vacuo. The primary rigid body modes of the sensor fall in a range of frequencies from 19.5 kHz-66.7 kHz. This is useful because it gives us a sense of the operational bandwidth of the device; it is expected that the device can be treated as a static structure up to at most 19 kHz for quasistatic operation, or perhaps bandwidth should be slightly lower (10-15 kHz). In addition, these modes may be a useful diagnostic as it is possible to measure the modal frequencies of the structure after processing to see if the device is behaving as expected.

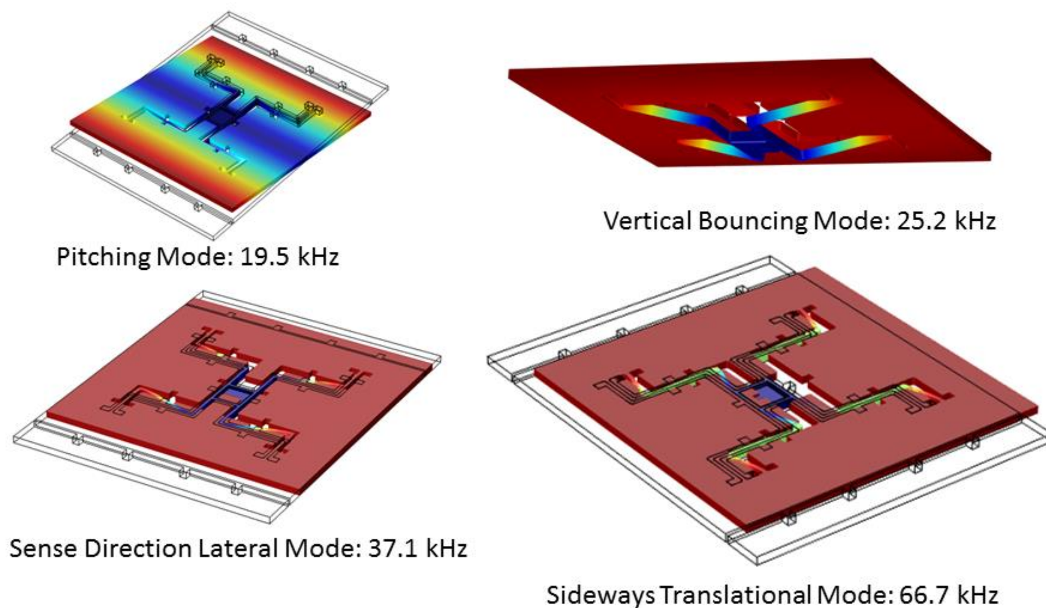

Figure 3-5 Modal analysis of shear sensor in vacuo. Each modal frequency is shown under each type of response.

Using the same properties from table 3.1 a model for static response due to a lateral load of 1 Pa was done in COMSOL. The total area of the shuttle is $1.31 \cdot 10^{-7}$ m^2 and a 1 Pa lateral load was applied over the entire top surface of the shuttle. The static displacement result can be seen in figure 3.6. The lateral motion of the shuttle is 0.21 nm/Pa towards the sense direction (toward the electrode walls). A moment also exists from this load case because the load is applied over the top surface which is offset from the neutral axis. The tilt displacement of the shuttle is 0.055 nm/Pa at the trailing edge with the trailing edge down. This corresponds to an angle of $1.6 \cdot 10^{-5}$ degrees. The total flow direction force and total moment from this study were $1.31 \cdot 10^{-7}$ N and $0.655 \cdot 10^{-12}$ N·m respectively. Knowing the force (F), moment (M), sensitive direction displacement

(x), and angle displacement (θ) due to a moment it is possible to determine structural stiffness in both the lateral (k_x) and pitch directions (k_θ). Equations for both can be seen in equations (3) and (4).

$$k_X = \frac{F}{x} = \frac{1.3 \cdot 10^{-7} N}{0.21 \cdot 10^{-9} m} = 624 N/m \tag{3}$$

$$k_\theta = \frac{M}{\theta} = \frac{0.66 \cdot 10^{-12} N \cdot m}{2.8 \cdot 10^{-7} rad} = 2.40 \cdot 10^{-6} \frac{N \cdot m}{rad} \tag{4}$$

Once stiffness values are calculated, using results from the COMSOL model, they may then be compared to an analytical estimate that is determined given the shuttle's beam geometry and material properties of Nickel. From equation (5), lateral stiffness estimates requires a young's modulus (E = 219 GPa), taken from table 3.1, the thickness of the structure (b = 10 μm), the width of the beam (h = 5 μm), and the length of the center crab leg beam (L = 100 μm). This is because during lateral displacement only the center crab leg beams experiences the most bending.

The stiffness due to a moment in the beam (equation (6)) requires the same young's modulus, width, and structural thickness. Two different beam lengths (denoted L_2 and L_3) are also needed. L_2 (205 μm) is the total length of the unwrapped crab leg since torsional displacement causes bending throughout the entire beam. L_3 is the moment arm need to calculate torsional stiffness (k_θ) and is taken to be from the center of the anchor to the end of one of the crab leg beams. Calculated stiffness values can be seen in table 3.2.

$$k_X \approx \frac{4Ebh^3}{L^3} \approx \frac{4(219GPa)(10 \cdot 10^{-6} m)(5.0 \cdot 10^{-6} m)^3}{(100 \cdot 10^{-6} m)^3} \approx 1000 \frac{N}{m} \tag{5}$$

$$k_\theta \approx \frac{4Ehb^3}{L_2^3} L_3^2 \approx \frac{4(219GPa)(5.0 \cdot 10^{-6} m)(10 \cdot 10^{-6} m)^3}{(205 \cdot 10^{-6} m)^3} (130 \cdot 10^{-6} m)^2 \approx 8.60 \cdot 10^{-6} \frac{N \cdot m}{rad} \tag{6}$$

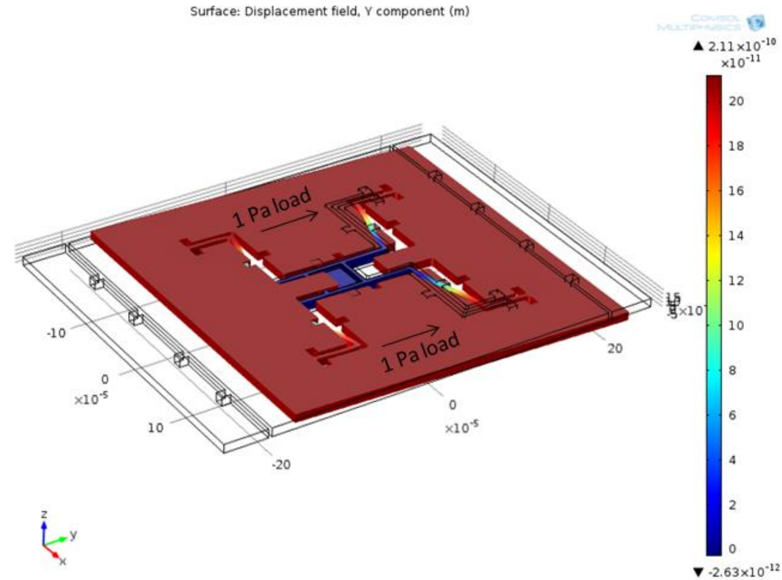

Figure 3-6 Static response of MEMS shear sensor in COMSOL. Solid mechanics model used a 1 Pa lateral load over the entire top surface of the shuttle. Material properties are shown in table 3.1. Lateral motion of the shuttle was 0.21 nm/Pa in the sense direction, and the shuttle tilt was calculated to be 0.055 nm/Pa with the trailing edge down.

Table 3-2 Summary of stiffness results (given model and analytical estimates), beam geometry values, force, displacement (tilt, lateral, and vertical) from COMSOL model.

	Value	Analytical Estimate (Stiffness only)	Units	Notes
F	1.31E-07		N	Force Due to 1 Pa Shear
x	2.10E-01		nm	Lateral Displacement Due to 1 Pa Shear
θ	2.80E-07		rad	Shuttle Tilt Due to 1 Pa Shear
z	4.40E-01		nm	Vertical Displacement Due to 1 Pa Shear
L	100		μm	Length of center crab leg beam (See Figure 3.4)
L2	205		μm	Total Length of Beam (Unwrapped Crab Leg)
L3	130		μm	Moment Arm (Center of Anchor to end of Crab Leg)
b	10		μm	Thickness of Shuttle
h	5		μm	Width of beams
K_x	624	1000	N/m	Lateral Stiffness
K_θ	2.40E-06	8.60E-06	N·m/rad	Tortional Stiffness due to Moment
K_z	298	508	N/m	Vertical Stiffness

A second static response model was studied in COMSOL focusing on the vertical displacement of the shuttle. Similar to the previous model, a 1 Pa vertical load was applied over the entire top surface of the shuttle. As mentioned before the area of the

shuttle is $1.31 \cdot 10^{7}$ m^{2}. As before, this allows for a total direction force of $1.31 \cdot 10^{-7}$ N given a 1 Pa load. From results the vertical motion of the shuttle was determined to be 0.44 nm/Pa in the vertical direction. Structural vertical stiffness (k_z) can be calculated from these values (see equation (7)) as well as an analytical estimate (see equation (8)) given beam geometries from table 3.2. During vertical displacement the entire length of the beam experiences some bending which is why L_2 is used. Stiffness results can be seen in table 3.2, and COMSOL results can be seen in figure 3.7. Analytical estimates only assume bending deformation in the shear sensor. Because the analytical model does not include torsion, shear, or elongation in any beam, stiffness values are higher than those in the COMSOL model.

$$k_z = \frac{F}{z} = \frac{1.31 \cdot 10^{-7} N}{0.44 nm} = 298 \frac{N}{m} \tag{7}$$

$$k_z \approx \frac{4Ebh^3}{L_2^3} \approx \frac{4(219 GPa)(5.0 \cdot 10^{-6} m)(10 \cdot 10^{-6})^3}{(205 \cdot 10^{-6} m)^3} \approx 508 \frac{N}{m} \tag{8}$$

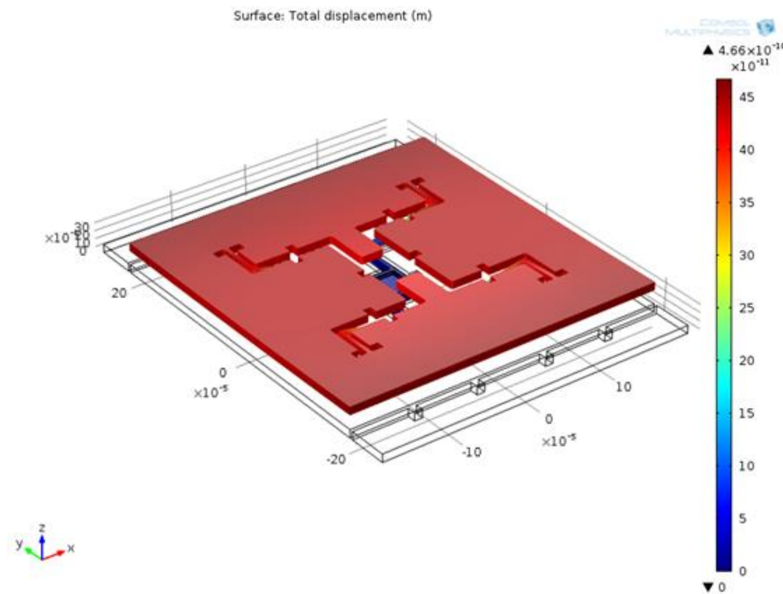

Figure 3-7 Static response of MEMS shear sensor in COMSOL. Solid mechanics model used a 1 Pa vertical load over the entire top surface of the shuttle. Material properties are shown in table 3.1. Vertical motion of the shuttle was 0.44 nm/Pa.

3.3.2 Electrostatic Modeling

Two electrostatic studies in COMSOL were used to determine static capacitance of each element. Each model is set up to be 2D, linear, and stationary with no deflection of the shuttle. The model includes only the shuttle and fixed electrode, both 10 µm thick, with a 5 µm wide sense gap between both structures. One study includes a 10 µm long electrode expansion underneath the element while the other does not. This electrode expansion is used to increase sensitivity of the shuttle, avoid problems associated with charging up the glass substrate, and increase uniformity during lithography. For current shear sensor devices this extension is implemented. A downside to the electrode expansion is an increase in static capacitance. For both studies a 1 V potential difference is applied between the shuttle and fixed electrode. Material properties for this study are identical to the ones in table 3.1.

The first study, which includes no electrode expansion, can be seen in figure 3.7. This study resulted in a total charge along the shuttle of $6 \cdot 10^{-11}$ C/m. For a 400 µm long shuttle (see figure 3-4) this results in a capacitance of 25 fF along each side of the shuttle and applies to each individual element. The second study, which includes a 10 µm long expansion under the shuttle, can be seen in figure 3.8. This study resulted in a total charge along the shuttle of $7.4 \cdot 10^{-11}$ C/m. For a 400 µm long shuttle this results in a capacitance of 30 fF along each side of the shuttle and applies to each individual element.

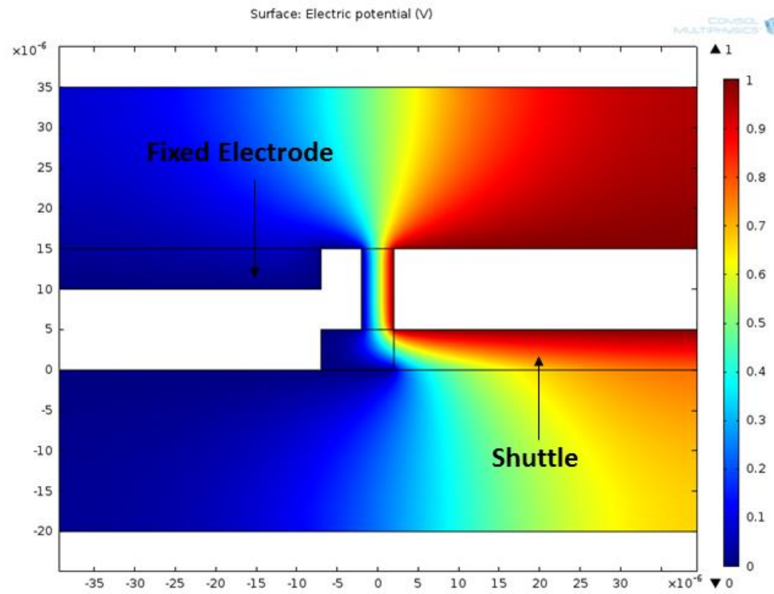

Figure 3-8 2D linear electromechanical study made in COMSOL. The gap between the shuttle and fixed electrode is 5 µm and both the shuttle and fixed electrode are 10 µm thick. This model includes a 1 V potential difference between the fixed electrode and shuttle. Results include a total capacitance of 25 fF for each individual element on either side of the shuttle.

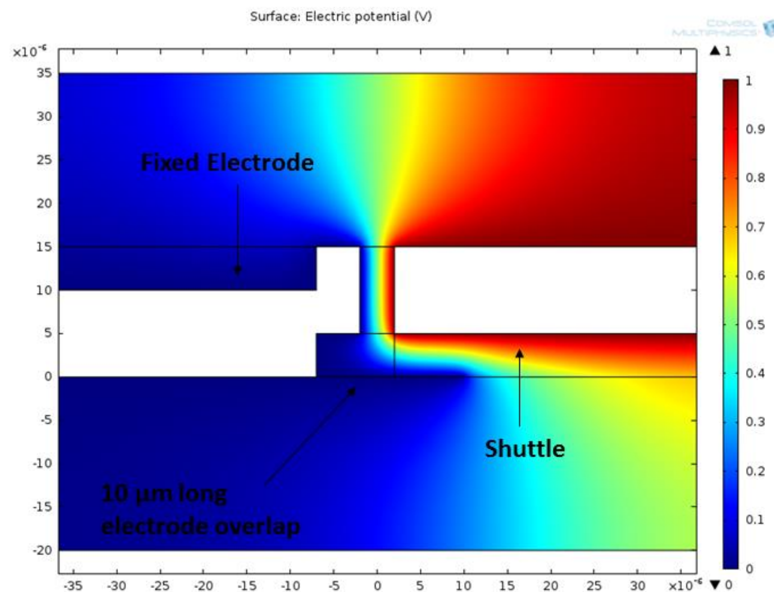

Figure 3-9 2D linear electromechanical study made in COMSOL. The gap between the shuttle and fixed electrode is 5 µm and both the shuttle and fixed electrode are 10 µm thick. This model includes a 1 V potential difference between the fixed electrode and shuttle and a 10 µm long electrode overlap underneath the shuttle. Results include a total capacitance of 30 fF for each individual element on either side of the shuttle.

Given the total static capacitance of each element and the number of elements in each group of the MEMS shear sensor device it is possible to determine the total static capacitance of each group for either side of the device. This is done by multiplying the total static capacitance of each element by the number of elements in each group. For shuttles with no electrode extension, Group A and C have a total static capacitance of 2.4 pF per side, while groups B and D have a total static capacitance of 1.2 pF per side. For shuttles with an electrode extension, Group A and C have a total static capacitance of 2.9 pF per side, while groups B and D have a total static capacitance of 1.4 pF per side. It is evident that the shuttles with the electrode extension exhibit higher static capacitance. A summary of these results can be seen in table 3.3.

Table 3-3 Summary of Results for 2D Linear Analysis of Static Capacitance Values of MEMS Shear Sensors

	Value	Units
Total Charge Along Shuttle (No Extension)	6.00E-11	C/m
Total Charge Along Shuttle (With Extension)	7.40E-11	C/m
Shuttle Length	400	µm
Total Static Capacitance on Each Side (No Extension) of Individual Element	25	fF
Total Static Capacitance on Each Side (With Extension) of Individual Element	30	fF
Number Elements in Groups A and C	96	
Number Elements in Groups B and D	48	
Total Static Capacitance of Groups A and C Per Side (With No Extension)	2.4	pF
Total Static Capacitance of Groups B and D Per Side (With No Extension)	1.2	pF
Total Static Capacitance of Groups A and C Per Side (With Extension)	2.9	pF
Total Static Capacitance of Groups B and D Per Side (With Extension)	1.4	pF

Using the same geometry as before for static capacitance models, additional simulation runs were implemented to study the effects of shuttle deflection on

capacitance measurements. Lateral, vertical, and rotational deflection of the shuttle the three degrees of freedom allowed for a rigid body in this symmetric load case were studied. In all studies only the most recent version of the shear sensor is studied which includes a 10 μm electrode extension underneath the shuttle. For lateral deflection each simulation run included moving the shuttle away further and further from the electrode each time. When the shuttle exhibits this type of lateral motion capacitance decreases. A plot, gathered from simulation results, of the change in capacitance of this side for each individual element vs. lateral deflection can be seen in figure 3-10. Data suggests that this relationship is linear. The change in capacitance per unit of deflection for lateral motion (S_x) is 3.19 fF/μm.

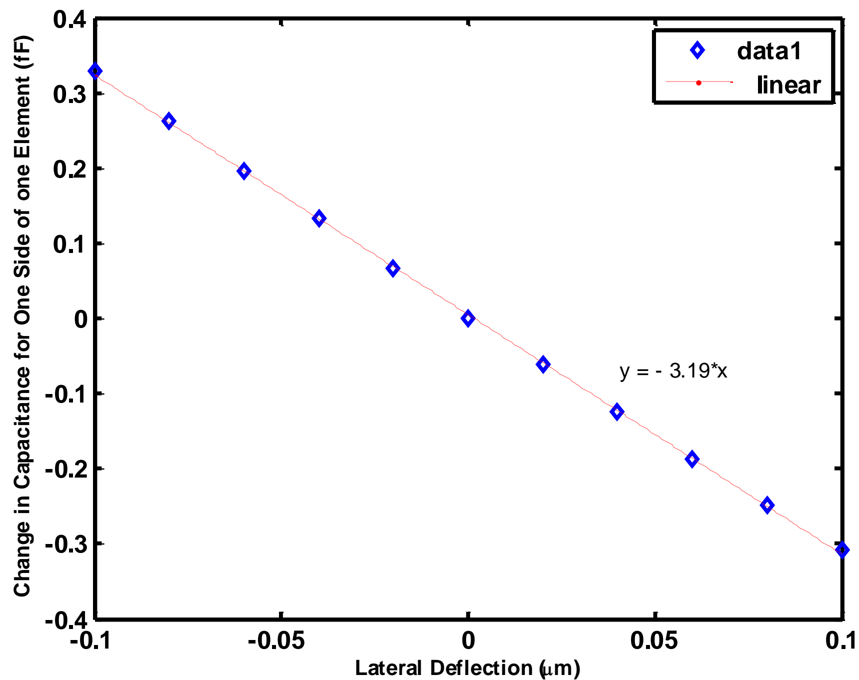

Figure 3-10 Change in capacitance for one side of one element (fF) vs. lateral deflection of the shuttle (μm). As the shuttle moves away from one of the fixed electrodes, causing an increase in lateral deflection, capacitance decreases. This data suggests that this relationship is linear and it may be approximated by the line y = -3.19x.

Vertical deflection was studied by moving the shuttle upwards away from the electrode small increments at a time. Results suggest that upward motion of the shuttle causes a decrease in capacitance. A plot of the change in capacitance of one side of one

element vs. vertical deflection can be seen in figure 3-11. This data is not as linear as the data for lateral or pitching motion since moving the shuttle upward or downwards is not symmetrical. However, the data may still be approximated by a linear fit. The change in capacitance per unit of vertical deflection (S_z) is 2.73 fF/μm for one side of one element.

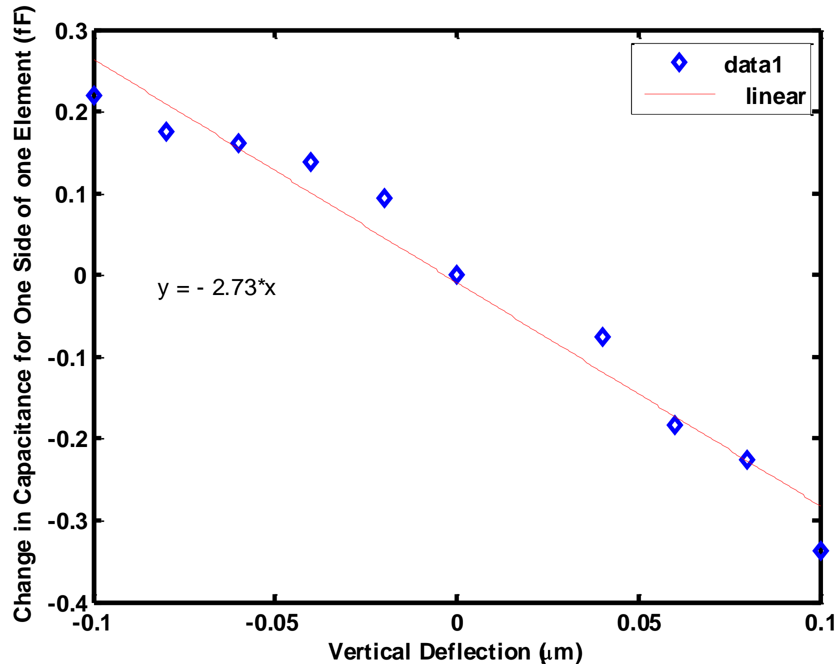

Figure 3-11 Change in capacitance for one side of one element (fF) vs. vertical deflection of the shuttle (μm). As the shuttle moves upward, causing an increase in vertical deflection, capacitance decreases. This data may be approximated with a linear fit with the line y = -2.73x.

For a rotation analysis the shuttle was moved by angle increments with one of the shuttle ends nose down. From results it is shown that capacitance increases on this side. A plot of the change in capacitance for this side of the shuttle for each element vs. pitching rotation can be seen in figure 3.12. This data may also be represented by a linear fit. The change in capacitance per unit of rotational deflection (S_θ) is 6.50 fF/deg. When differential capacitance measurements are taken during device testing it is possible to determine deflection of the shuttle as well as get an idea for what type of deflection is occurring by referring back to these model results. A summary of these results can be seen in table 3-4.

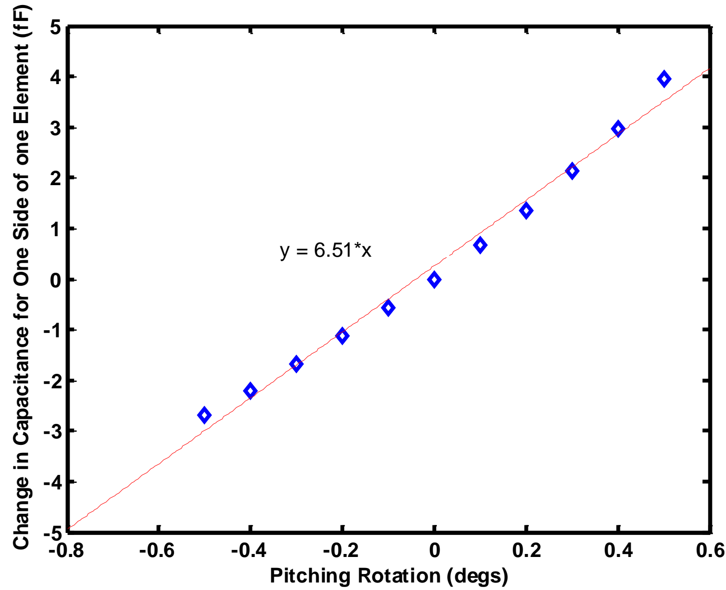

Figure 3-12 Change in capacitance for one side of one element (fF) vs. pitching rotation of the shuttle (deg). As the modeled end of the shuttle moves downward capacitance increases. This data may be approximated by the line y = 6.51x.

Table 3-4 Change in Capacitance for modeled side of element in COMSOL. Linear fit data based on figures 3.10, 3.11, and 3.12.

Motion	Change in Capacitance/Deflection	Units	Linear Fit
Lateral (S_x)	-3.19	fF/μm	y=-3.19x
Veritcal (S_z)	-2.73	fF/μm	y=-2.70x
Pitch (S_θ)	6.50	fF/μm	y=-6.51x

3.3.3 Fluids Modeling

Structural modeling allowed us to make stiffness predictions of this MEMS shear sensor device. Electrostatic modeling has allowed us to predict differential capacitance given no deflection and some deflection of the shuttle. In order to tie all models together, models that have been implemented separately, an additional fluids model was created in order to determine both total aerodynamic loading of the device as it undergoes flow in a duct. The duct used represents the laminar flow cell test set up that was created by Zhengxin for testing of previous shear sensor models. The influence of flow on the device will cause a force and moment on the shuttle, based on the shuttle's stiffness the shuttle will exhibit certain deflection, this deflection then influences the electrostatics of

the MEMS shear sensor. By combining results from all models it is possible to determine how well this shear sensor is capable of measuring flow in this scenario.

This 2D fluids model assumes linear behavior, incompressible flow, as well as laminar flow. The fluids model can be seen in figure 3.13. Poiseuille flow is assumed in from the left with a flow rate of air of 30 cubic feet per hour (CFH), the duct is 300 μm high (h), and the length of the channel is 28 mm long (l). The average fluid density (ρ) and average dynamic viscosity (μ) of air is taken to be 1.204 kg/m^3 and $1.814 \cdot 10^{-5}$ Pa·s respectively. A 10 μm thick structure with a 5 μm air gap underneath the shuttle represents the MEMS Shear Sensor in this model.

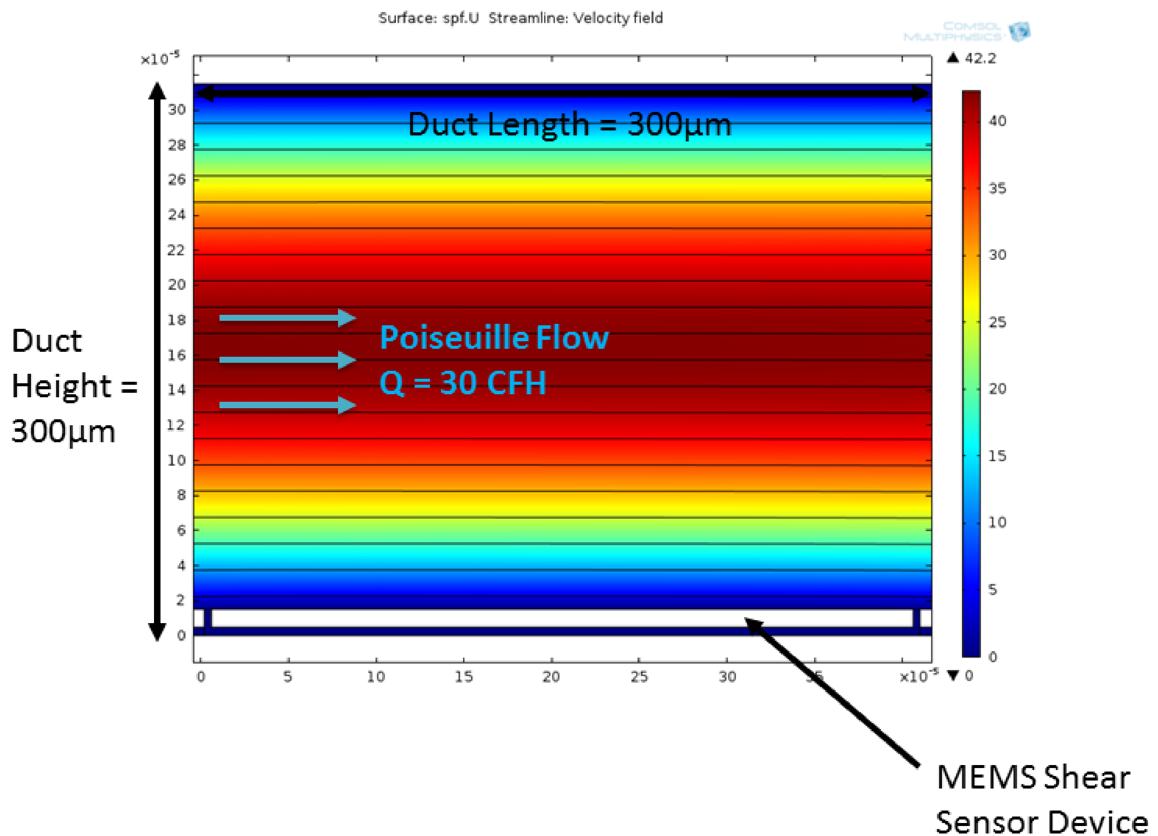

From this model the computed total aerodynamic force on the element is made up of three force components. Flow direction force, F_x, is computed to be 1.74 μN, lift force, F_z, is computed to be -0.041 μN, and pitching moment, F_θ, is computed to be $-2.15 \cdot 10^{-11}$ N·m. This characterizes the shear force as being downstream, pushing down towards the substrate, and pitching nose down. A summary of model parameters and results can be seen in table 3.6.

Table 3-5 Fluids Model Parameters and Force Results

	Value	Unit
Flow Rate (Q)	30	CFH
Duct Height (h)	300	μm
Duct Length (l)	28	mm
Avg. Fluid Density (ρ)	1.204	kg/m^3
Avg. Dynamic Viscosity (μ)	1.81E-05	Pa·s
Flow Dir. Force (F_x)	1.74	μN
Lift Dir. Force (F_z)	-0.041	μN
Pitch Dir. Force (F_θ)	-2.15E-11	N·m
Shear Sensor Thickness	10	μm
Air Gap Under Released Structure	5	μm

From these forces it is possible to determine how much the shuttle deflects in the flow, lift, and pitch directions given a fluid flow rate (Q = 30 CFH) and previously determined stiffness values from structural models (k_x = 624 N/m, k_z = 298 N/m, k_θ = $2.4 \cdot 10^{-6}$ N·m/rad). Deflections, for this flow case, are expected to be 2.8 nm downstream, 0.14 nm down towards the substrate, and $9.0 \cdot 10^{-6}$ degrees nose down which results in an additional edge deflection 0.03 nm on top of the vertical deflection. It should be noted that these deflections are less than 0.1% of the gap, justifying linear assumptions and an uncoupled fluid-structure model.

3.3.4 System Modeling

From previous testing results it is known that sensitivity of the shear sensor to both wall shear and a pressure gradient exist from fluid flow. This is taken into consideration when thinking about the fluids model discussed in the previous chapter. Using force results from the fluids simulation (F_x, F_z, F_θ) a connection may be made to model the MEMS shear sensor system in order to determine both sensitivities. In the true case, the sensor responds to the full aerodynamic load, which is not as simple as a pure shear and pure pressure gradient. Further study is needed to justify that assumption for various flow scenarios. In order to be clear about what we mean by "shear sensitivity" and "pressure gradient sensitivity" the assumptions made in deriving these two integrated quantities are described.

In many flows we might expect these to be the two dominant types of interaction. The first assumption is that sensitivity to wall shear may be computed by applying a pure mechanical shear only to the top surface of the element. This will require using results only from the structural and electrostatics model. The second assumption is that that any additional sensitivity observed in a full fluid mechanics model can be attributed to pressure gradient effects. This will require combining results from the fluids, electrostatic, and structural models. Confirmation of this methodology will be made in future experiments where the sensor will undergo flow in a laminar flow cell.

The following outlines a procedure for how to determine both sensitivity values given results from previously described COMSOL models:

1. Using results from the structural mechanics model and electrostatic models the sensitivity due to shear ($S_w = \frac{\Delta C}{\tau_w}$) may be determined.
2. From fluid flow modeling total change in capacitance due to all aerodynamic forces present may be determined (T).
3. Using what is known about Poiseuille flow and geometry of the modeled duct the shear sensitivity contribution may be subtracted from T. The resulting additional change in capacitance $P = T - S_w \cdot \tau_w$ is assumed to be due to a pressure gradient, where τ_w is the wall shear for Poiseuille flow.

4. Thre pressure gradient sensitivity is then $S_{dp/dx} = P/(\frac{\partial P}{\partial x})$ where $\frac{\partial P}{\partial x}$ is again known for Poiseuille flow.

Deflection results (see chapter 3.3.1) from the shuttles response to pure shear (τ_w = 1 Pa load) resulted in 0.21 nm/Pa of lateral motion (x), and $1.6 \cdot 10^{-5}$ deg/Pa of rotational motion (θ) with one end of the shuttle rotating downwards; we observe rotating motion is the load applied on the surface is offset from the central position of the shuttle (anchor region). Since vertical motion of the shuttle results in a common mode during differential capacitance measurements, change in capacitance in this direction is near zero, thus this motion may be ignored. From electrostatic models (see chapter 3.3.2) the change in capacitance due to lateral motion (S_x) and the change in capacitance due to rotational motion (S_θ) were 3.19 aF/nm and 6.5 fF/deg respectively.

$$S_{wx} = x \cdot S_x = (0.21\frac{nm}{Pa})(3.19\frac{aF}{nm}) = 0.67 aF / Pa \quad (9)$$

$$S_{w\theta} = \theta \cdot S_\theta = (1.60 \cdot 10^{-5}\frac{\deg}{Pa})(6.5\frac{fF}{\deg}) = 0.10 aF / Pa \quad (10)$$

Using equations (9) and (10) this results in a lateral shear stress sensitivity (S_{wx}) of 0.67 aF/Pa, and rotational shear stress sensitivity ($S_{w\theta}$) of 0.10 aF/Pa. This sensitivity only accounts for one side of the element, thus it is necessary to account for both sides by multiplying these values by a factor of 2 since there are two sense gaps in the element for differential capacitance measurements. Finally, total sensitivity is determined for each group by multiplying by the number of elements in the group with those resulting values. For groups A and C this results in a total sensitivity (S_{wAC}) of 0.15 fF/Pa and for groups B and D this results in a total sensitivity (S_{wBD}) of 0.074 fF/Pa. A summary of these results can be seen in table 3.6.

Table 3-6 Summary of Total Expected Sensitivity in all Groups of Shear Sensor Device

	Value	Units
Lateral Motion (x)	0.21	nm/Pa
Rotational Motion (θ)	1.60E-05	nm/Pa
Lateral Sensitivity for One Element and One Side (S_{wx})	0.67	aF/Pa
Rotational Sensitivity for One Element and One Side ($S_{w\theta}$)	0.1	aF/Pa
Lateral Sensitivity for One Element and Both Sides ($2 \cdot S_{wx}$)	1.34	aF/Pa
Rotational Sensitivity for One Element and Both Sides ($2 \cdot S_{w\theta}$)	0.2	aF/Pa
Number of Elements In Group A and C	96	
Number of Elements In Group B and D	48	
Total Expected Sensitivity in Group A and C (S_{wAC})	0.15	fF/Pa
Total Expected Sensitivity in Group B and D (S_{wBD})	0.074	fF/Pa

Recall from fluids modeling (see chapter 3.3.3) that the flow rate (Q) for 2D laminar poiseuille flow was set to be 30 CFH, the duct height (h) was set to 300 μm, the duct length was set to 28mm, and the dynamic viscosity of air (μ) was set to $1.81 \cdot 10^{-5}$ Pa·s. Given these parameters the pressure gradient ($\frac{\partial P}{\partial x}$) and shear stress ($\tau_w$) was determined to be -68 Pa/mm and 10.2 Pa respectively. These calculations are shown in equations (11) and (12).

$$\frac{\partial P}{\partial x} = \frac{-12\mu Q}{h^3 l} = \frac{-12(1.81 \cdot 10^{-5} Pa \cdot s)(30CFH)}{(300\mu m)^3 (28mm)} = -68Pa/mm \quad (11)$$

$$\tau_w = \frac{6\mu Q}{h^2 l} = \frac{6(1.81 \cdot 10^{-5} Pa \cdot s)(30CFH)}{(300\mu m)^2 (28mm)} = 10.2Pa \quad (12)$$

From fluid models three forces: F_x, F_z, and F_θ were computed (see chapter 3.3.3). Given these forces, stiffness values from structural models, a fluid flow rate of Q = 30 CFH, and poiseulle flow, calculations for deflection in the flow direction (x_p = 0.27 nm/Pa) and deflection in the pitch direction ($\theta_p = -5.03 \cdot 10^{-5}$ deg/Pa) can be seen in equations (13) and (14). From these deflection values capacitance values for the flow, lift, and pitching directions may be determined by multiplying x and θ, by their respective sensitivities due to motion determined from electrostatic models (S_x = 3.19 fF/nm and S_θ = 6.50 fF/deg). Calculations are shown in equations (15) and (16). From these calculations, total sensitivity due to shear and a pressure gradient in the flow direction, T_x, is 0.67 aF/Pa and sensitivity due to shear and a pressure gradient in the pitch direction, T_θ, is 0.33 aF/Pa. A summary of these results is given in table 3.7

$$x_p = \frac{F_x}{k_x \tau_w} = \frac{(1.74\mu N)}{(624\frac{N}{m})(10.2Pa)} = 0.27\frac{nm}{Pa} \tag{13}$$

$$\theta_p = \frac{F_\theta}{k_\theta \tau_w} = \frac{(-2.15 \cdot 10^{-6} N \cdot m)}{(2.4 \cdot 10^{-6}\frac{N \cdot m}{rad})(10.2Pa)(\frac{180}{\pi})} = -5.03 \cdot 10^{-5}\frac{\deg}{Pa} \tag{14}$$

$$T_x = x_p \cdot S_x = (0.27\frac{nm}{Pa})(3.19 fF / nm) = 0.035\frac{aF}{Pa} \tag{15}$$

$$T_\theta = \theta_p \cdot S_\theta = (-5.03 \cdot 10^{-5}\frac{\deg}{Pa})(6.50\frac{fF}{\deg}) = 0.33\frac{aF}{Pa} \tag{16}$$

Table 3-7 Motion and sensitivity due to shear and a pressure gradient in flow and pitch directions given 2D laminar poiessuille flow.

	Value	Unit
Flow Dir. Motion Given Duct Flow (x_p)	0.27	nm/Pa
Pitch Dir. Motion Given Duct Flow (θ_p)	-5.03E-05	deg/Pa
Sensitivity Due to Shear and a Pressure Gradient in Flow Dir. (T_x)	0.67	aF/Pa
Sensitivity Due to Shear and a Pressure Gradient in Pitch Dir. (T_θ)	0.33	aF/Pa

Given T_x and T_θ the total sensitivity due to shear and a pressure gradient in each group of the device may be determined by taking the sum of T_x and T_θ and multiplying that result, T, by the number of elements in a given group. The total sensitivity given a flow duct with a height 300 µm, length of 28 mm, laminar 2D flow rate of 30 CFH, is 0.19 fF/Pa for groups A and C (T_{AC}), and 0.096 fF/Pa for groups B and D (T_{BD}). These results are close to results from models where fluid flow in a duct is not considered (combination of structural and electrostatic models only). These results are summarized in table 3.8.

Table 3-8 Total Sensitivity due to shear, total sensitivity each group of the MEMS shear sensor from a combination of fluids, electrostatic and structural model.

	Value	Unit
Total Sensitivity due to Shear ($T = T_x + T_\theta$)	1	aF/Pa
Total Sensitivity in Groups A and C ($T_{AC} = 2 \cdot T \cdot 96$ elements)	0.19	fF/Pa
Total Sensitivity in Groups B and D ($T_{BD} = 2 \cdot T \cdot 48$ elements)	0.096	fF/Pa

Assuming that the difference between T_w and S_w is the response due to a pressure gradient sensitivity it is possible to estimate the sensitivity due to the pressure gradient in all groups (P_{AC} and P_{BD}) by equations. Compared to the previous shear sensor generation

the sensitivity due to a pressure gradient has significantly decreased while the sensitivity due to shear has shown improvement. This is credited to the new design which involves less surface topology and gaps throughout the device. A summary of predicted sensitivities from both a pressure gradient and shear stress as well as previously determined sensitivities from the older shear sensor generation is seen in table 3.9. It is important to note that the sensitivity values from the older generation have been determined from test results [2].

$$P_{AC} = \frac{T_{AC} - S_{wAC}}{\frac{\partial P}{\partial x}} = \frac{0.19 fF - 0.15 fF}{-68 \frac{Pa}{mm}} = -0.6 \frac{aF}{(\frac{Pa}{mm})} \quad (17)$$

$$P_{BD} = \frac{T_{BD} - S_{wBD}}{\frac{\partial P}{\partial x}} = \frac{0.096 fF - 0.074 fF}{-68 \frac{Pa}{mm}} = -0.3 \frac{aF}{(\frac{Pa}{mm})} \quad (18)$$

Table 3-9 Pressure gradient and shear stress sensitivities for all groups of current design and previously determined shear stress and pressure gradient sensitivity from the [2].

	Symbol	Value	Units
Pressure Gradient Sensitivity (Groups A&C)	P_{AC}	-0.60	aF/(Pa/mm)
Pressure Gradient Sensitivity (Groups B&D)	P_{BD}	-0.30	aF/(Pa/mm)
Shear Stress Sensitivity (Groups A&C)	S_{AC}	0.15	fF/Pa
Shear Stress Sensitivity (Groups B&D)	S_{BD}	0.07	fF/Pa
Previous Generation Shear Stress Sensitivity		-16.0	aF/(Pa/mm)
Previous Generation Pressure Gradient Sensitivity		0.08	fF/Pa

4 Fabrication

This section focuses on the surface micromachining process for these MEMS floating element shear stress sensors done at the Tufts Micro and Nano Fabrication Lab. This four mask process includes the following: A Chromium and Gold layer for electronic interconnects necessary for measurements, a Ti/Cu seed layer needed for subsequent plating of a thick copper sacrificial layer, and finally a thick plated nickel structural layer. After all layers are patterned, the copper sacrificial layer is etched out, releasing the devices. Images of the sensor undergoing the process will be shown, as well as comments regarding past and future changes to the microfabrication process. Finally, SEM images of the most recently released structures will be included in the discussion. The entire process is summarized in figure 4-1.

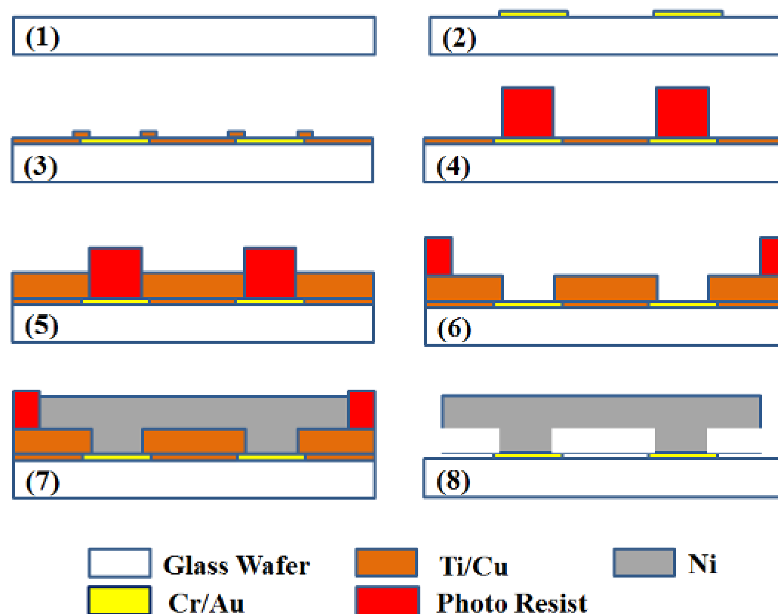

Figure 4-1 Overview of the surface micromachining process for the fabrication of these MEMS shear sensors. Steps are summarized as: (1) Starting glass substrate. (2) Deposition of Cr/Au (Metal Mask). (3) Deposition of Ti/Cu seed layer (Anchor Mask). (4) Lithography necessary for Cu plating (Anchor Mask). (5) Thick layer of Cu Plating (Sacrificial Layer). (6) Lithography necessary for Ni plating (Structure Mask). (7) Nickel plated layer. (8) Release of floating elements.

4.1 Chromium and Gold Metal Layer

The process begins by cleaning a 100±.2mm Soda Lime glass substrate that is 550±50µm thick. The substrate includes rounded edges, a primary flat, and a double sided polish. The wafer is first introduced to a ten minute piranha clean that is made up of two equal parts of Sulfuric Acid (96% by volume H_2SO_4) and Hydrogen Peroxide (30% by volume H_2O_2), and two three minute rinses in deionized water (DI). A 200 W Oxygen plasma at a 300 mT process pressure and 100 sccm gas flow rate is used to further clean the glass substrate for 120 seconds in a MARCH CS1701F Reactive Ion Etcher (RIE).

For this first deposition a 10 nm thick sputtered Chromium (Cr) layer and 70 nm thick sputtered Gold (Au) layer is deposited to form the necessary interconnects. Gold is used for its excellent conductive properties, and Chromium is used as an adhesion layer since Gold cannot adhere to glass on its own. This layer is thinner than previously fabricated (75/225 nm thick [2]) Cr/Au layers. This was done intentionally in order to reduce the residual stress occurring in these films that was causing delamination of Cr/Au (see chapter 5).

Most steps are similar to the previous fabrication process [2] and are outlined as the following:

1. Lift off Resist (LOR20B) is spun onto the wafer at 2000 rpm for 45 seconds in a Laurell WS-400B-6NPP-Lite Manual Spinner which is then followed by a 5 min softbake on a hotplate, with no tinfoil, at 200ºC. This LOR20B resist typically forms a 2 µm thick layer under these settings. Similarly, a different resist, AZ9260, is spun on another Laurell spinner for 60 seconds at 6000 rpm. This is then followed by a 2 minute softbake on a hotplate, with tin foil, at 115ºC. After measurements in a Bruker DekTak XT Profilometer thicknesses of this AZ9260 resist is typically around 7-8 µm.

2. Using an OAI Model 204IR Aligner, the substrate undergoes a 30 second hard contact exposure under UV light, forming the pattern for this metal Cr/Au layer.

3. The pattern is then developed using a solution of one part AZ400K developer to 3 parts DI water for about 2 minutes and 20 seconds with mild agitation followed by two DI water rinses each two minutes long. The wafer is then air dried and inspected. The developing time may vary due to laboratory conditions (temperature or humidity changes), and if more developing time is needed a new batch of solution is used.

4. Prior to deposition, the wafer is placed in the March RIE in a 200 W Oxygen plasma at a 280 mT process pressure and 100 sccm flow rate for 60 seconds. This is done to remove any unwanted photoresist particles introduced during lithography.

5. Using a NSC3000 DC powered Sputter Tool a 10 nm thick Cr film is deposited using a DC power supply of 200 W. This is immediately followed by a 70 nm thick Au film deposition using a DC power supply of 120 W. Approximate deposition rates for each deposition are 3.0 A/s, and 6.0-7.0 A/s respectively. Both films are deposited using an Argon gas process pressure of 5 mT, however, due to recent discovery of a possibly faulty pressure gauge, or errors in pressure calculations in LabVIEW this pressure may be higher or lower than recorded (see chapter 6).

6. A liftoff is required to achieve final desired features for this Cr/Au film. This is achieved by placing the wafer in heated remover 1165 in a glass petri dish. The remover is heated via a hotplate operating at 80ºC in order to achieve a 60ºC solution temperature. The glass petri dish is covered, and the wafer is left in this heated remover for over three hours, in some cases overnight. After enough time has passed, the wafer is quickly removed to a fresh batch of Remover 1165 so that it may be sonicated for five minutes. This lift off removes a lot of material, thus sonicating helps to remove any unwanted particles. After sonicating for five minutes the wafer undergoes two three minute DI water rinses before being air dried and prepared for the next lithography. Measurements are done using the

DekTak in order to see if thickness measurements agree with the sputter tool. Generally results are very close to the desired 80 nm, varying slightly from the center of the wafer to the edge (see chapter 5).

Images of sputtered Cr/Au layers can be seen in figure 4-2. In hopes of thickening the Cr/Au layer while also maintaining low stress films, recent runs of this process includes Cr/Au films that have been evaporated at Harvard University's clean room (see chapter 5).

Figure 4-2 MEMS shear sensor interconnects necessary for capacitance measurements. This layer consists of 10 nm of DC sputtered Chromium and 70 nm of DC sputtered Gold.

4.2 Seed and Sacrificial Layers

The seed layer consists of Titanium (30 nm) and Copper (300 nm) and is necessary for Copper plating. 5 μm of Copper are plated onto the seed layer and form a sacrificial layer between the Nickel and seed layer. This step has undergone a few changes from the original micromachining process since high quality Ti/Cu seed layer films are necessary for the successful plating of Cu in the next step. With the original low-quality Ti/Cu films from the NSC3000, the films typically failed by delaminating during copper plating.

1. A similar lithography process as mentioned previously is done for the Ti/Cu seed layer. The only difference is that a longer 3 minute and 30 second develop time is used compared to the previous 2 minute and 20 seconds. LOR20B is spun onto the wafer followed by the spinning of AZ9260 and a 2 minute softbake at 115ºC. Thicknesses of each photoresist are 2.0 µm, and 7-8 µm respectively. After exposing the surface with UV light for the same amount of time (30 seconds with hard contact), developing with mild agitation, using DI water rinses, and air gun drying the wafer is prepared for Ti/Cu deposition. Images after the second lithography can be seen in figure 4-3.

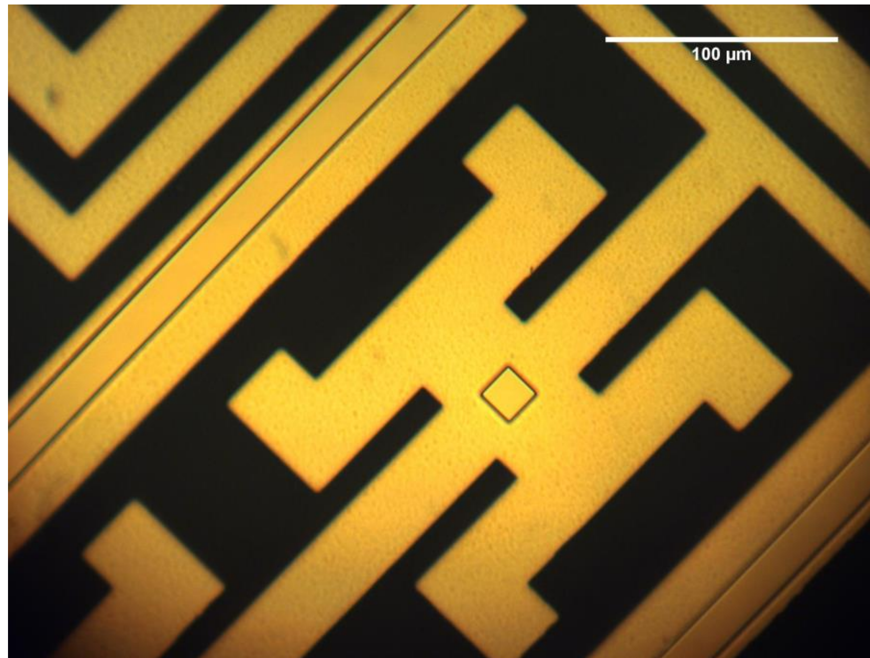

Figure 4-3 Close up of shear stress sensor after the second lithography. The anchor and fixed electrode regions will be exposed after a Ti/Cu lift off.

2. As before, a 200 W Oxygen plasma at a flow rate of 100 sccm and a 280 mT process pressure is introduced to the wafer in the March RIE tool in order to remove any unwanted photoresist residue.

3. **Original Process:** Using the NSC3000, 30 nm of Titanium at a DC power supply of 200 W is deposited, followed by 300 nm of Copper at a DC power supply of

150 W. For both cases a 5 mT process pressure of inert Argon is used for sputtering. Here, the Ti serves as an adhesion layer for Cu. The deposition rate for Ti is 2.8-3.3 A/s and the deposition rate for Cu is 6.0 A/s.

Thick Copper Sputter: Using the NSC3000, 50 nm of Titanium at a DC power supply of 200 W was deposited followed by a thick 4 µm Copper sputter deposition also at 200 W. For both films deposition occurred at a process pressure of 5 mT. The deposition rates were 2.5 A/s for Ti and 5.0 A/s for Cu. More on this in Chapter 5.

Evaporated Ti/Cu: Current processing includes an evaporated Ti/Cu layer with 30 nm of Ti at a deposition rate of 1.0 A/s and 300 nm of Cu at a deposition rate of 3.2 A/s

4. The same lift off procedure with heated remover 1165 is used as done for the Cr/Au lift off. Images after liftoff can be seen in figure 4-4. The final result looks good, however, after a few failed attempts at Cu plating on top of this Ti/Cu layer, alternatives to this stage of the process has been investigated (see chapter 5). Suspicion points to potential contaminants in the NSC3000 that could be the cause of poor films and thus a poor sacrificial layer. The problem was solved by depositing these films at Harvard CNS using evaporation.

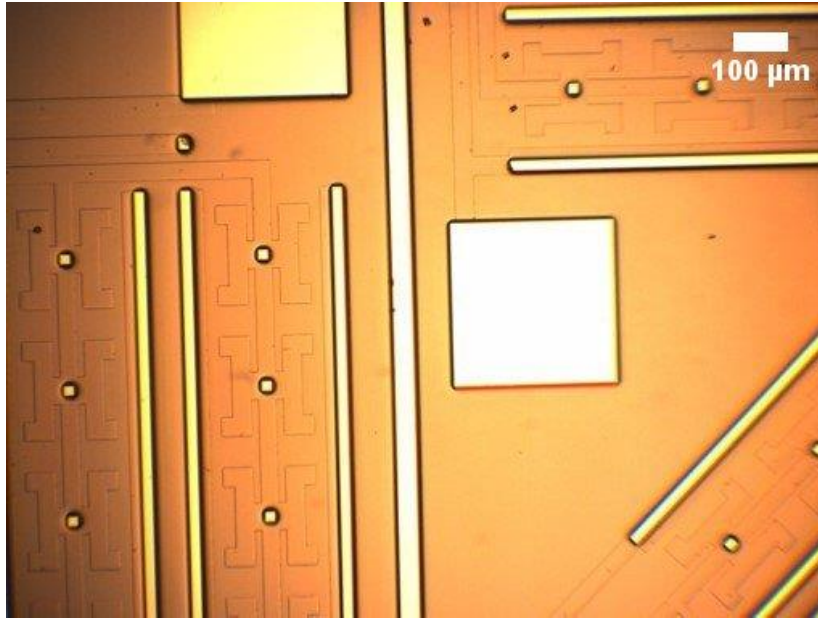

Figure 4-4 Final Ti/Cu 30/300 nm sputtered seed layer after liftoff in heated remover 1165 (60ºC). Poor Cu plating on this film has led to alternatives such as evaporation deposition at Harvard University's clean room, the attempt of a thick Cu sputter, and the addition of a SiO_2 passivation layer (more on this in chapter 5).

5. The third lithography in this process differs from the first two as it prepares the wafer for Cu plating (this is not done if there is a thick Cu sputter of 4 µm). LOR20B is no longer needed since this thicker Cu layer will not be lifted off in heated remover, and instead will be wet etched away to release the Nickel layer that will be plated on top of it. For this step HMDS (Hexamethyldisilazane) primer is spun onto the wafer to improve the adhesion of AZ9260 that is spun afterwards. Both the primer and photoresist are spun at 3000 rpm for 60 seconds in a Laurell spinner. Spinning is followed by a 3 minute softbake at 120ºC.

6. Using the OAI Contact Aligner the wafer is exposed in UV light for 35 seconds under hard contact.

7. Developing time in AZ400K and DI water (1:3 ratio) is usually around 5 minutes, again varying depending on environmental conditions in the lab. More agitation is used than before since thicker resists require it for uniformity. This develop is

followed by two DI water rinses before the wafer may be air gun dried. A thickness of about 6 µm is expected under these conditions.

8. Prior to Cu plating the wafer undergoes the typical Oxygen plasma descum procedure.

9. As done in Zhengxin's previous work a coper sulfate plating solution named "Acid Copper Semi-bright" from Technic Inc, Cranston, RI is used to plate 5 µm of Copper. A current density of 5 mA/cm^2 is set up to achieve a 130 nm/min deposition rate. For a 30 minute plating time 390 mA is used on a wafer area of 78 cm^2. This is conducted at room temperature with continuous filtration using a recirculating filter in the tank. Recent processing modifies this process to a homemade solution of a Cu plating bath that is made up of 0.8 M of Copper Sulfate, and 1.5 M of Sulfuric Acid that has about 70 ppm of Chloride Atoms. The plating current density was also increased to 15 mA/cm^2, resulting in a higher quality film and a higher deposition rate of approximately 300 nm/min.

10. After plating, the wafer is placed in a five minute acetone soak, followed by a 2 minute isopropanol soak, and two 2 minute DI water rinses. This is done to strip the AZ9260 photoresist.

11. Photoresist residue is common after Cu plating. To fully remove this residue an Oxygen plasma descum (cleaning of photo resist residue) is used on the wafer.

4.3 Structural Nickel Layer and Release of Floating Elements

A 10 µm thick Nickel plated layer is used as the structure for the floating element. Release of this structure has proven to be more difficult than in the past. Extra focus has been spent on the seed, sacrificial, and structural layers, as well as the introduction of different drying methods (see chapter 5) in order to have properly released elements.

1. HMDS Primer and AZ9260 is spun onto the wafer, this time at 1000 rpm for 60 seconds. After spinning, the wafer undergoes a 4 minute softbake at 120ºC.

2. The wafer undergoes a 25 second exposure, 5 minute developing time in AZ400K and water, two 2 minute DI water rinses and is air gun dried.

3. An Oxygen plasma descum is performed.

4. Since Copper tends to oxidize over some time, the wafer is dipped in a 10% Sulfuric Acid solution for 1 minute. The wafer is then rinsed for a minute and immediately placed into the Nickel plating solution.

5. The Nickel Sulfamate solution is heated to 50ºC prior to plating. A 100 nm/min deposition rate is achieved with a 5 mA/cm^2 current density set by a 160 mA current. After 100 minutes of plating a target thickness of 10 µm is achieved. For better uniformity the wafer is usually taken out of the plating solution after 50 minutes. Different points on the wafer are measured via the DekTak to check on the status of the deposition rate. The wafer is flipped (flat side up if flat was down before or vice versa) and placed back into the Ni plating solution for the remaining 50 minutes. Images of the shear sensor after Nickel plating can be seen in figure 4-5. Recently, this process was updated to use higher current densitiy (15 mA/cm^2), and a 54ºC solution temperature achieved using a closed loop immersion heater. This appears to improve Ni film quality. Deposition rate also increased to 300 nm/min.

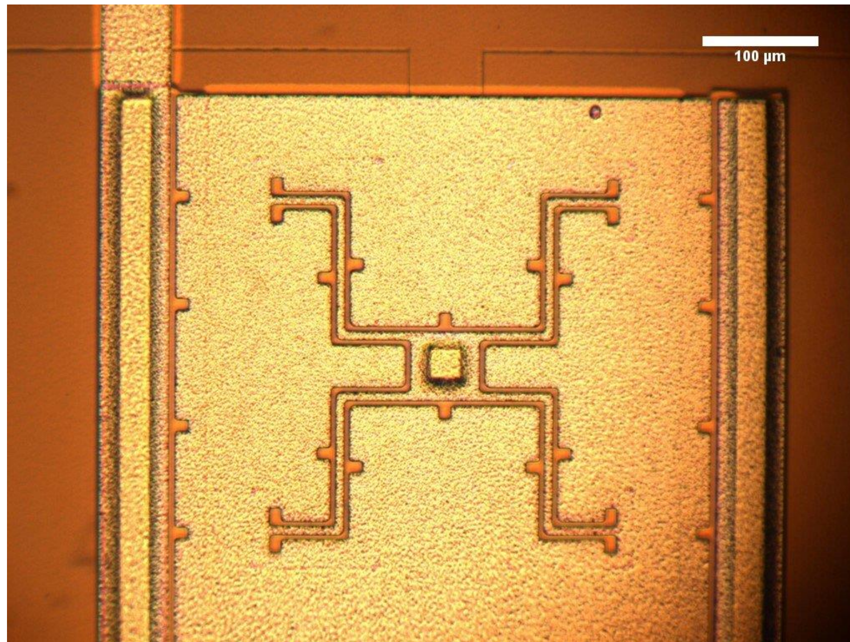

Figure 4-5 MEMS shear sensor post Ni plating.

6. After plating the same photoresist strip is done as was done after Cu plating.

7. Prior to dicing the structural layer is protected by spinning on HMDS and AZ9260 at 3000 rpm for 60 seconds. A softbake of 4 minutes at 120ºC completes the protective layer of photoresist for the wafer against the dicing saw.

8. An MA1006 dicing saw is used to dice the wafer into individual 1 cm^2 chips.

9. The protective photoresist layer is stripped by soaking the thermal adhesive and shear sensor chips in a dish of acetone. Foil is placed in the dish prior to the acetone to prevent chips from sticking to the bottom of the petri dish. From the acetone soak the chips begin to come off of the thermal adhesive as the adhesive is dissolved away. The individual dies are moved quickly into an IPA solution for 5 minutes followed by two 5 minute DI water rinses. From here, each individual die is then dried off one by one using an air gun.

10. A few dies are then chosen to undergo a 200 W, 120 second Oxygen plasma clean at 100 sccm in a 280 mT RIE chamber. From here chips are placed in either the

Tousimis carrier to later be critically point dried, or a separate carrier to later be air dried in a box.

11. In either case the carrier is placed in a copper wet etch solution consisting of a 1:1:18 ratio of Acetic Acid (CH_3COOH): Hydrogen Perioxide (H_2O_2): DI water for 1-7 days. Release etches of two days or less may not be sufficient to fully release devices; the Titanium etches very slowly. After sufficient release time has been reached the carriers are moved into two 10 minute DI water rinses, a 10 minute IPA soak, and 30 minute Methanol soak to prepare the chips for the final drying step. At this point the Ti/Cu seed layer and Cu structural layer has been etched away, releasing the Ni structural layer.

12. Chips are either left in a dry box with reduced relative humidity for at least two hours, or dried in a Tousimis critical point drier.

Images of chips that have undergone the whole process can be seen in figure 4-6. Beam and gap widths can be seen in figure 4-7, and sense gap widths can be seen in figure 4-8. Further discussion in chapter 5 will be focused on the changes to these micromachining steps in hopes of optimizing the process.

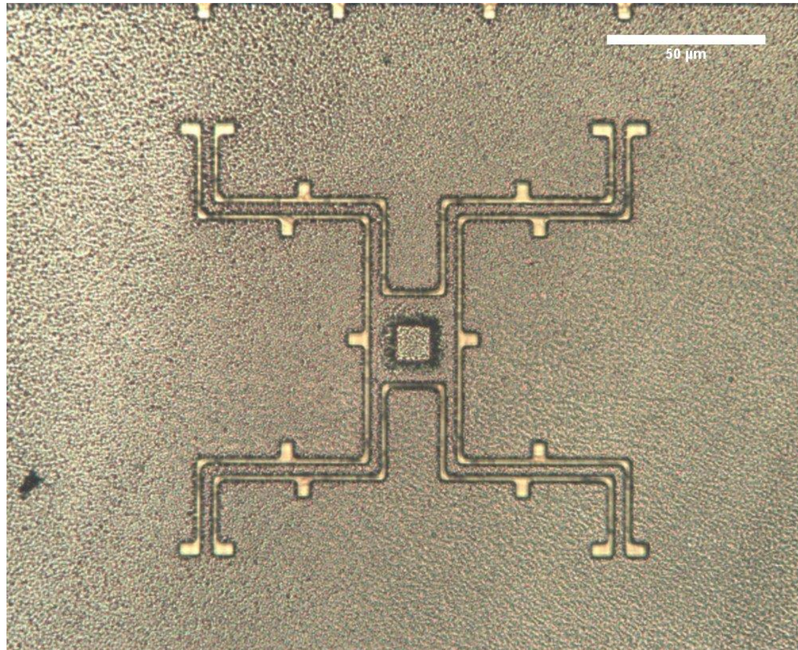

Figure 4-6 Image of MEMS shear sensor at the end of the surface micromachining process.

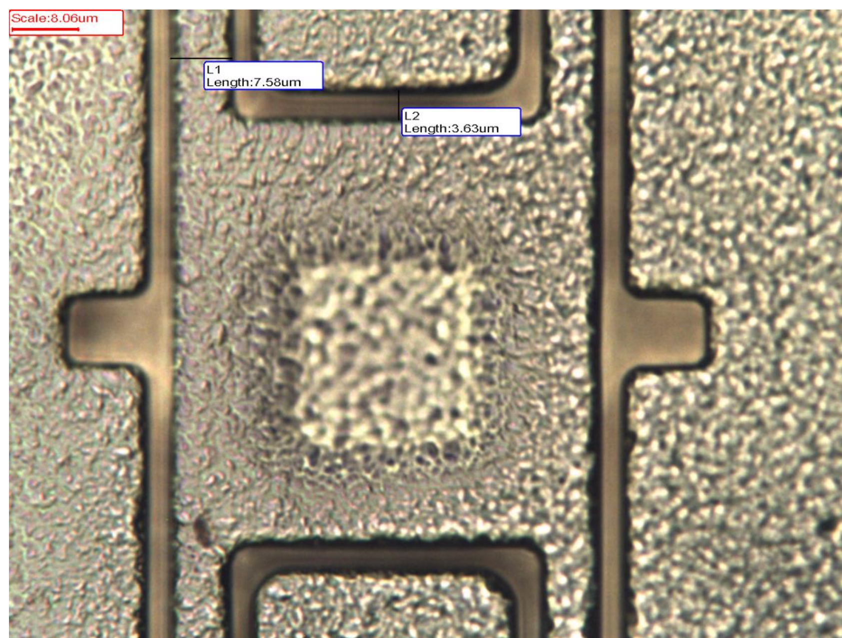

Figure 4-7 A close up image near the anchor region shows the beam length of the shear sensor (L1 = 7.56 µm) and beam gap (L2 = 3.63 µm). Scale bar = 8.00 µm.

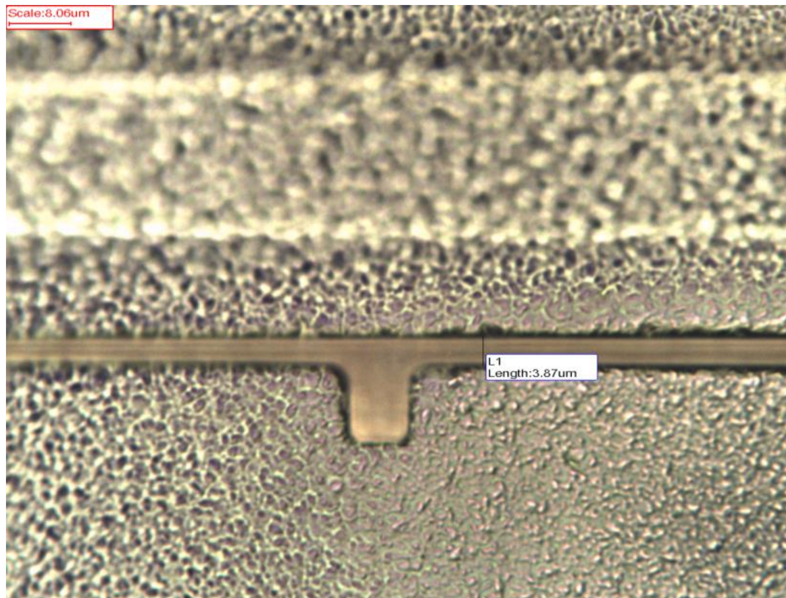

Figure 4-8 A close up image of the sense gap (L1 = 3.87 μm) between the floating element and one of the fixed electrodes is shown. Scale bar = 8.00 μm.

4.4 SEM Images

The following SEM images come from recent fabrication runs. A major difference to note is how the sacrificial layer was deposited. Due to issues in Copper plating a thick 4 μm Cu layer was sputtered. These images show chips that have been released with this change. Figure 4-9 shows an element (from either group B or D) to show how some of the major components of the element looks like after fabrication is completed. Figure 4-10 shows a close up of one of the elements' beams from the same chip. Figure 4-11 shows a close up of the sense gap, also from the same chip.

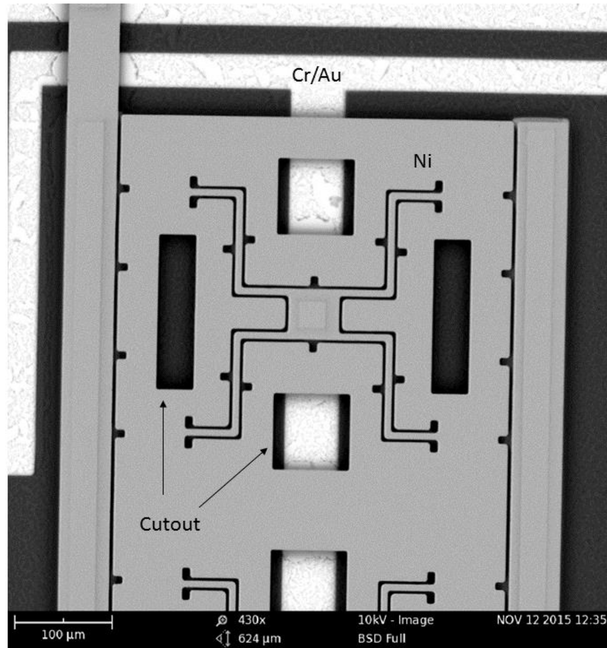

Figure 4-9 SEM image of shear sensor with cut outs (Group B or D)

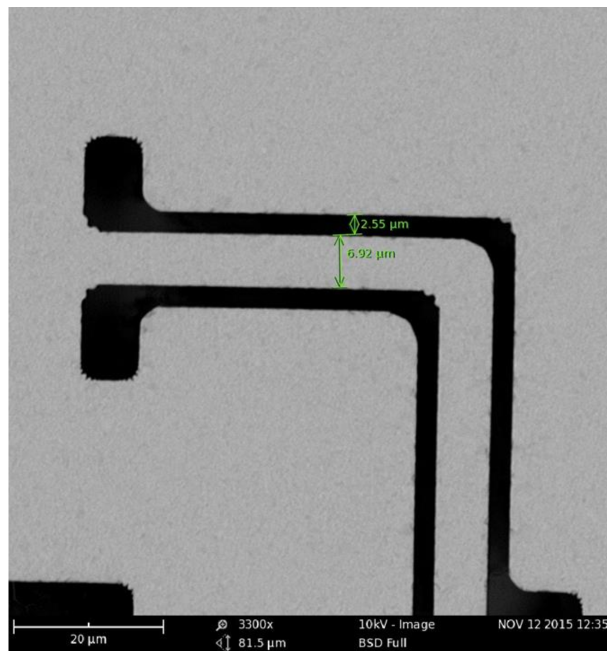

Figure 4-10 SEM image of beam width (6.92 µm) and beam gap width (2.55 µm).

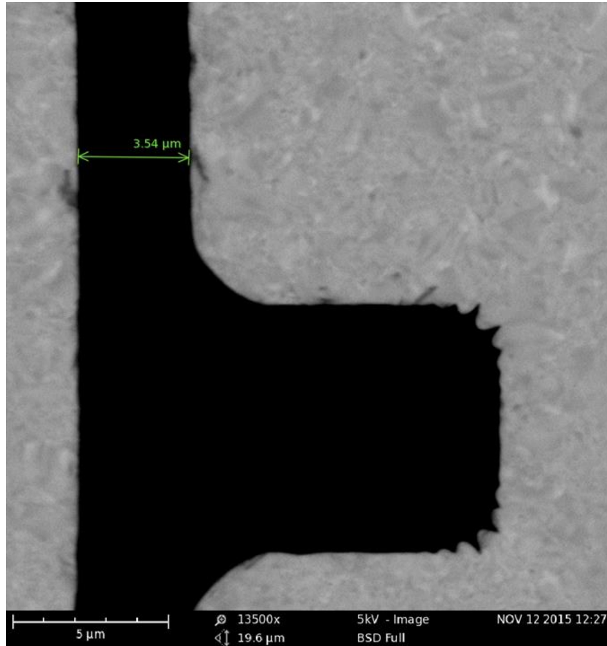

Figure 4-11 SEM image of sense gap width (3.54 µm). Here the sense gap is smaller than the desired 5 µm.

5 Changes to the Fabrication Process

In order to achieve working devices, many changes and experiments relating to the surface micromachining process have been performed. These changes are driven by the pursuit of elements that are not stuck down and high quality low stress films. It is interesting to note that the original fabrication process has worked in the past, and allowed for the development of MEMS sensors that were able to undergo calibration and testing [2]. Recent delamination of films, poor Copper and Nickel plated films, and stiction may be due to contamination of organics in the deposition tools, particularly the NSC3000 sputter tool. Many of the problems have been solved by moving to ebeam evaporators at Harvard CNS, however challenges persist in achieving high quality lithography for the last, and structural nickel step.

5.1 Change of Process Thickness of Cr/Au Layers and Stress in Multilayered Films

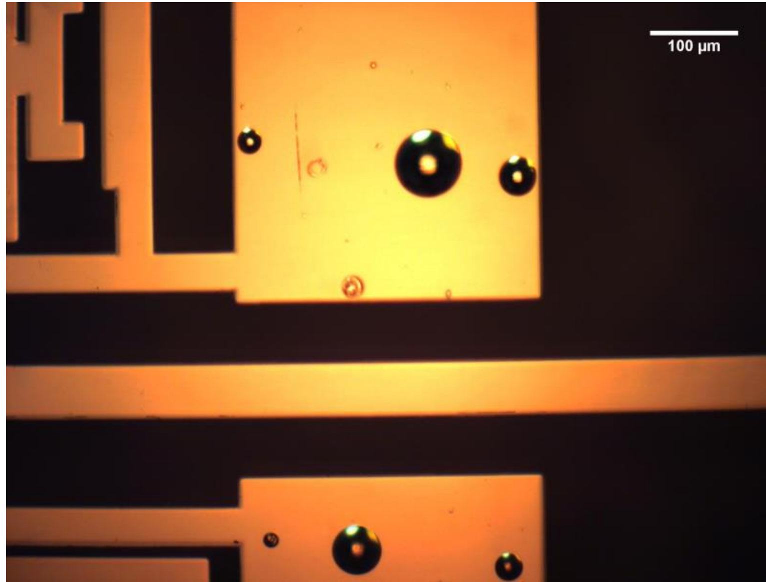

Figure 5-1 Image of film defects on Cr/Au (75/225 nm) after sputtering at 5 mT.

After getting a few wafers past the first metal layers of Cr/Au using original thickness values of 75 nm of Cr and 225 nm of Au, it was observed in many wafers that sputtering had caused blisters to form on the surface of both films (see figure 5.1). A close up of a blister can be seen in figure 5.2. These blisters are caused by compressive residual stresses within the Cr and Au films that cause the films to buckle. As mentioned in the literature, under enough compressive stress these blisters may buckle further causing the blisters to extend into "telephone cord" or "worm" like features [7]. Sputtering causes different crystalline structures to form within films and these structures vary depending on what process pressure, power, and gas is used. Other factors such as the thickness and the thermal coefficient mismatch of multilayered films also affects the amount of residual stress that occurs. Other factors may include base pressure within the chamber, the exposure to contaminates that may cause undesirable alignment of metal atoms (intrinsic stresses), and chamber temperature [8].

Figure 5-2 Image of Cr/Au blister caused by compressive stress within the multi layered film.

There is always some residual stress within thin films, thus optimization of process parameters is necessary in order to create the best films possible given a certain tool. Three different parameters were varied for the deposition of many Cr/Au films in the NSC3000 sputter tool. They are: process pressure, Cr/Au thickness, and DC power supplied to the target guns. Similar to Tan and Miao's study [8], the hope was to recreate their experiments with the Tufts Micro and Nano Fabrication's own sputter tool by varying one of the parameters and keeping the others constant and then measuring the stresses occurring in the films using Stoney's Equation for microscope slides [9] (See equation (19). The stress in the film is determined knowing the thickness of both films (t_f), the young's modulus of the substrate (E_s), the thickness of the substrate (h), the poison's ratio of the substrate (v_s), and the radius of curvature of the substrate after the deposition of both films (R^s). Values for E_s, h, and v_s are summarized in Table 5.1.

T_f had a tendency to vary after each deposition especially since some radial thickness variation occurs within the NSC3000 (see Chapter 6). The thickness of each slide was measured by marking off four locations on the slide with a sharpie, depositing Cr/Au, and then lifting off the metal by placing the slide in acetone. The average thickness of each of the four locations determined t_f. R^s was calculated by measuring the radius of curvature before and after deposition. An alternative equation can be seen in equation (20) where R_{pre} is the curvature before deposition and R_{post} is the curvature after deposition [10]. Other factors in this experiment include base pressure, platen rotation

speed, target to substrate distance, and type of substrate (75 mm x 25 mm x 1 mm microscope soda lime glass slides); these factors were held constant for all experiments.

$$\sigma_f t_f = \frac{E_s h^2}{6(1-v_s)R^s} \tag{19}$$

For the first set of experiments process pressure was chosen as the first variant. The end goal was to measure the center stress of the substrate containing 10 nm of sputtered Cr and 70 nm of sputtered Au. These thickness values were chosen based on Tan and Miao's study where they found this ratio of Cr/Au to be optimal in their experiments [8]. Three case studies were chosen for this pressure experiment. Case 1 included an Argon process pressure of 3 mT, case 2 included a pressure of 5 mT, and case 3 used 7 mT of pressure. A total of 27 microscope slides were measured on a DekTak XT Stylus Profilometer and careful alignment of each slide was taken into consideration for stress measurements (See figure 5.3).

Table 5-1: Properties Microscope Soda Lime Glass Slides

*Taken from [11]

**VWR Microscope Slides (75x25x1 mm^3)

Young's Modulus (E_s)	Thickness of Substrate (h)	Poisson's Ratio (V_s)
72 Gpa*	1000 µm**	.23*

Each slide was numbered, and a laser cut marked alignment slide (See Appendix) made of acrylic was used to load each slide properly. Positioning of each slide is critical for good results since in order to achieve good comparison between curvatures for each slide (both pre and post curvatures) it is necessary to have the Dektak scan along the same length and start and end at the same location each time. The alignment slide was used to set up where the stylus needed to start for each scan. On the Dektak stage two alignment pins were also used to center the slide of interest and positioning was held in place by three adjacent dummy slides. Parameters of each scan can be seen in Table 5.2.

$$\sigma_f t_f = \frac{E_s h^2}{6(1-v_s)}\left(\frac{1}{R_{Post}} - \frac{1}{R_{\mathrm{Pr}e}}\right) \tag{20}$$

Due to inconsistencies in data (see Chapter 6) three slides were taken, one from each case, and measured again. This time each slide underwent ten scans each. Five of those scans included taking the slide out and realigning it before each scan, and the other five scans included leaving the slide loaded without realignment. Comparisons were made between both methods in hopes of finding a better way to measure curvature (see Chapter 6).

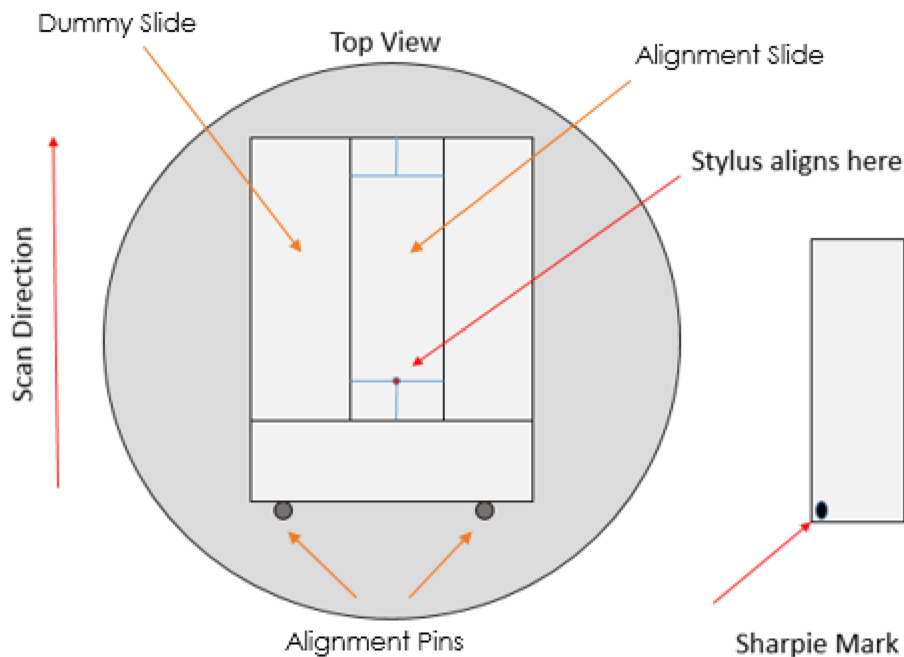

Figure 5-3 Top view of the alignment configuration for curvature measurements using a Bruker Dektak XT Stylus Profilometer. Three dummy slides were used to center the alignment slides and slides of interest as well as two alignment pins from the Dektak's stage. Markings were used on the alignment slide to set the start and end of each scan. Each test slide was marked with a sharpie.

Due to continuing inconsistencies using microscope slides, additional measurements were made on three four inch <100> Silicon wafers. Each of the three wafers underwent similar deposition conditions as the slides, and each wafer represented one of the previously described pressure cases. E_s, v_s, and h values are shown in Table 5.3. Using wafers eased alignment configurations in the Dektak since the stage has alignment pins suited for wafers. Each wafer underwent twenty scan measurements. Five of those twenty scans included unloading and loading the wafer each time with the wafer held down with vacuum provided by the stage. Another five scans included no

unloading prior to measurements. An additional five scans included unloading and loading the wafer each time with ball bearings placed on the stage underneath the wafer to allow for more relaxed bending in the substrate. Finally, another five scans included measuring the wafer with bearings, but without unloading and loading prior to each scan. Chapter 6 summarizes results for all curvature measurements. These results have changed the Cr/Au process thickness to 10 nm of Cr and 70 nm of Au. Thicker metal layers can be achieved in an evaporator since the evaporation process tends to experience less residual stress [8].

Table 5-2 Dektak Scan Parameters for Curvature and Stress Measurements

Range	Stylus Radius	Profile	Scan Time	Stylus Force	Scan Length
1 mm	12.5 µm	Hills and Valleys	45 Seconds	8 mg	55000 µm

Table 5-3 Material Properties of <100> Silicon Wafer

Young's Modulus (E_s)	Thickness of Substrate (h)	Poisson's Ratio (V_s)
169 GPa*	550 µm**	.28*

5.2 Seed and Copper Layer

After success in removing stress blisters in the Cr/Au layers, processing continued past the sputtered Ti/Cu seed layer, and Copper plating steps. However, unlike in the past, after Copper plating with usual parameters the Cu layer failed to adhere to the Ti/Cu properly and delaminated as shown in figure 5.4. A few changes were made to combat these issues: a thick Cu sputter process to avoid Cu plating all together, and evaporating a Ti/Cu layer prior to attempting Cu plating at Harvard CNS.

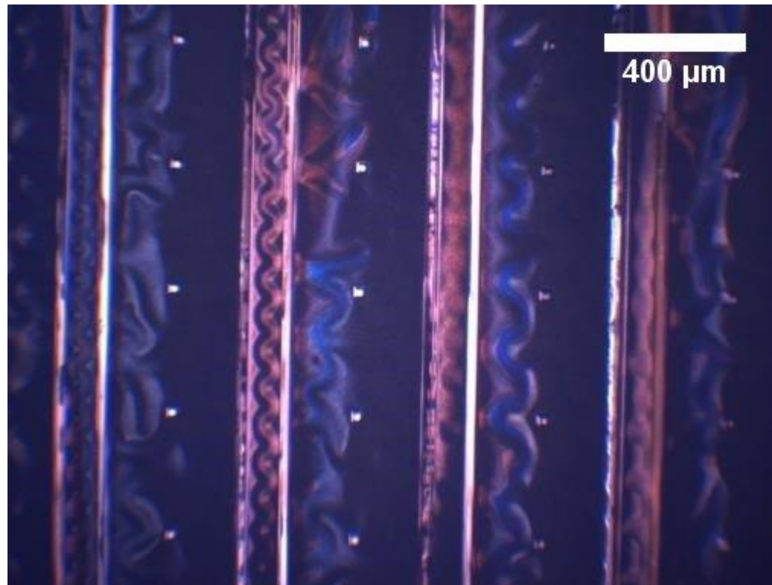

Figure 5-4 Failed Cu plated layer. Worm like and telephone chord like features are due to high compressive residual stress that cause delamination.

Using the NSC3000 a thicker 50 nm Titanium layer was deposited at 200 W and with an Argon process pressure at around 5-6 mT. Following this deposition, a thicker 4 µm Copper layer was deposited at 200 W and with a 5-6 mT Argon pressure. Deposition rates were 2.5 A/s and 5.0 A/s respectively. To avoid drawing too much power for too long, power supplies were turned off 30 minutes into the deposition for 15-20 minutes and restarted up again for the remaining time. This deposition takes much longer than usual sputtering jobs, about an hour total, however, a thicker Cu layer avoids an additional lithography step, and plating step[2].

After processing wafers with a thick Cu sputtered sacrificial layer many defects were found along the way. It is suspected that these defects may have been the cause of floating elements experiencing stiction (see Chapter 6). Considering the problems that occurred previously with the Cr/Au layers, and issues with a defected seed and sacrificial layer, it was suspected that the NSC3000 may have contaminated substances that deposit onto the substrate during deposition. This is most likely due to the fact the sputter tool is shared with other lab groups; some of which deposit metal onto organic substances. In addition, the base pressure in the NSC3000 is very poor; at best it is in the 10^{-4} Torr range.

Recent attempts at processing includes removing sputtering all together, and depositing evaporated Cr/Au and Ti/Cu films in a cleaner chamber at Harvard CNS. 30 nm of Ti and 300 nm of Cu was deposited after pumping down the chamber at 1.20×10^{-6} Torr. Deposition rates of Ti and Cu were 1.0 A/s and 3.2 A/s respectively. Images of these films can be seen in Chapter 6.

5.3 SiO_2 as a Passivation Layer

This past summer the Tufts Micro and Nano Fabrication Lab acquired a new Sputter deposition tool named the Angstrom NexDep. This chamber has been selected to deposit only a limited amount of materials in hopes of keeping the chamber environment more controlled. Currently, two targets have been purchased for the tool; Aluminum (Al) and Silicon Dioxide (SiO_2). After experiencing stiction in some wafers that were processed with thick sputtered Cu films, a new process involved depositing a 100 nm thick RF sputtered SiO_2 film after the Cr/Au interconnects were set in place in 5 mT of Argon gas pressure. The hope was that with a layer of SiO_2 on top of the electrical interconnects of the shear sensor it could act as a protective barrier from a contaminated Ti/Cu layer. One of the disadvantages to this process is the addition of a lithography and deposition step. SiO_2 deposits very slowly having a dep rate of .2 A/s which also makes the process lengthy. Results of these experiments are discussed in chapter 6.

6 Experimental Results

This chapter presents experimental results from fabrication changes that are discussed in chapter 5. Focus will be spent on stress calculations in Cr/Au film on both glass slides and 4 inch Silicon wafers, results on thick Ti/Cu sputtering, results from evaporated Cr/Au and Ti/Cu films, and finally results from RF sputtering SiO_2. In all cases these attempts were pursued in order to improve the quality of films and reduce the possibility of stiction of the Nickel floating element during release.

6.1 Stress in Cr/Au Films

Stress calculations in 10 nm/ 70 nm of Cr/Au at three different process pressures (3 mT, 5 mT, 7 mT), were made to see the effect of pressure on sputtered film. Results indicate that either the process is inconsistent in between runs, or using a Stylus Profilometer to make curvature measurements is inconsistent in between measurements, or both. This was first observed after measuring the center stress of 27 Cr/Au samples. Figure 6.1 shows data on the center stress of slides vs. various process pressures. From this data it is shown that at each process pressure stress is inconsistent and varies at a large range. From this data, and other data gathered from similar measurements, it was concluded that slide data was not repeatable.

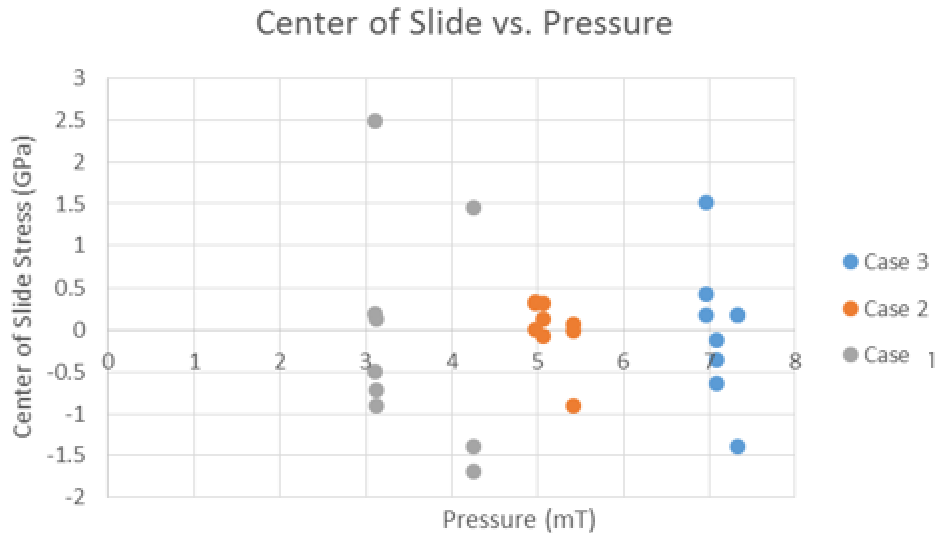

Figure 6-1 Center of Slide Stress (GPa) vs. Process Pressure of Cr/Au film. Case 1 = process pressure of 3 mT, Case 2 = process pressure of 5 mT Case 3 = process pressure 7 mT

Despite an attempt to control conditions during the sputtering process, data has shown large inconsistency in residual stress in slides (and in other tests with Silicon Wafers). From data it was shown that moving wafers and slides in between measurements may contribute a large amount to stress variation, despite attempts for proper alignment each time. However, even without moving anything unwanted noticeable variations continue to exist. From data it is also shown that large differences in stress occur in measurements done with bearings compared to those without. This is attributed to free movement of the wafer on bearings during measurement that plays a role in determining curvature. Aside from measurement conditions, sputtering conditions are also of a concern. From inconsistent data it is also possible to conclude that in between each sputtering deposition the process pressure may not be as controlled as desired. This will be shown later when discussing issues during thick Ti/Cu sputtering.

6.2 Thick Ti/Cu Sputtering

Figure 6-2 50 nm/ 4 µm of sputtered Ti/Cu in the NSC3000 sputter tool.

Thick sputtering was attempted in hopes of replacing Copper plating steps of the surface micromachining process after failed Cu plated film was observed (See Chapter 5). In figure 6.2 an image of 4 µm thick Copper on a 50 nm thick Titanium layer is

shown. At a glance the film looks clean and uniform, however, upon closer inspection, dark residue is observed around the boarders of most features (See Figure 6.3).

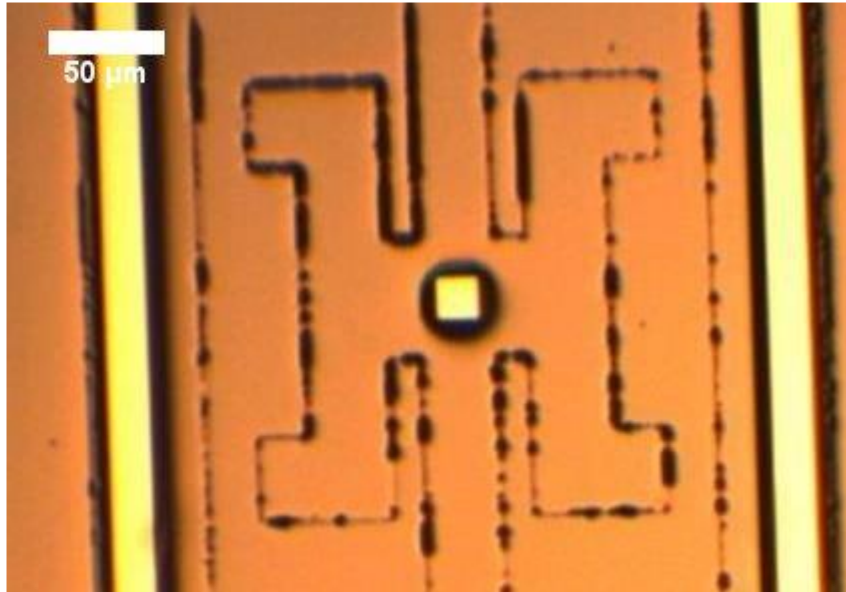

Figure 6-3 Residue observed around the edges of some features after the thick Ti/Cu sputter

It was at first believed that this residue had come from photoresist. The wafer underwent some O_2 plama descums and a lift off process to relieve the issue. Despite these cleaning attempts residue remained. In order to see the effects of the residue these wafers were still processed to the end especially since despite the residue, there were no signs of delaminated Cu film. From this thick sputtered Cu it was possible to plate Nickel once again and continue with the micromachining process past the release stages.

On released dies resistance was measured for all for groups to determine if the floating element was stuck down. This was done using metal probes, sending a 1kHz signal through the probes, driving that signal at 1 Volt, with a zero DC bias. By placing the probes on one pad wired to one of the fixed electrodes, and the other on another pad wired to the floating element, it is possible to measure the resistance between that connection. A low resistance (in the Ohm range) is considered to be undesirable since it indicates that the element is stuck down. A higher resistance (in the MΩ and GΩ range) indicates that the element is suspended above the surface since air underneath the element is a large insulator that increases the resistance between the floating element's electrical connections and the fixed electrode. For all measurements each electrode was measured

with the floating element separately to determine a top and bottom resistance. Very few groups exhibited released floating elements indicating that all structures were stuck down after release. Table shows data on some chips; more detailed data tables can be seen in appendix C.

Table 6-1 Resistance and Capacitance data on released MEMS Shear Sensors. These sensors underwent a thick 5 μm sputtered copper deposition. Most elements exhibited low resistance values indicating that the floating element is stuck down. More data on other chips can be seen in Appendix 3.

Top/Bottom Electrode	Group	Resistance	Device Capacitance With Stray Cable Capacitance Subtracted Out	Other Data	Process
Bot	A	100 Ω	Short	Chip 6	Thick Cu Sputter (5μm)
Top	A	117 Ω	Short	Chip 6	Thick Cu Sputter (5μm)
Bot	D	69 Ω	Short	Chip 6	Thick Cu Sputter (5μm)
Top	D	1 GΩ	6 pF	Chip 6	Thick Cu Sputter (5μm)
Bot	C	143 Ω	Short	Chip 6	Thick Cu Sputter (5μm)
Top	C	160 Ω	Short	Chip 6	Thick Cu Sputter (5μm)
Bot	B	123 Ω	Short	Chip 6	Thick Cu Sputter (5μm)
Top	B	276 Ω	Short	Chip 6	Thick Cu Sputter (5μm)

In order to inspect the chip further and gain insight of what may have caused stiction of these elements, the top Nickel layer was stripped from a few groups. From inspection it was found that all elements had grainy residue underneath the Nickel layer (See Figure 6.4). Recalling the residue from the thick Cu sputter, speculation regarding the sputter process arose. From SEM images (See Figure 6.5) grainy residue is still evident. From the same SEM tool a chemical analysis study confirmed that the grainy residue contained carbon content. This clarified some speculation that the residue was organic and its source was most likely from the NSC3000 sputter tool since the tool has housed organic materials in the past.

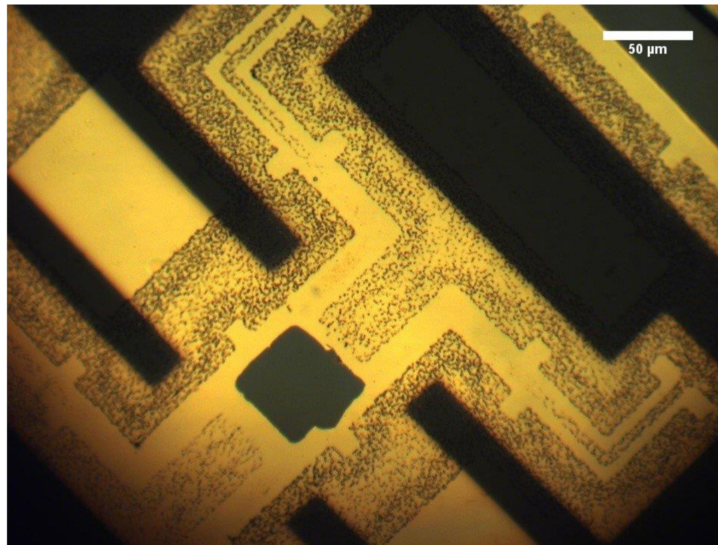

Figure 6-4 Grainy residue observed underneath Nickel film. Residue surrounds boarders similar to those observed after thick Ti/Cu sputtering

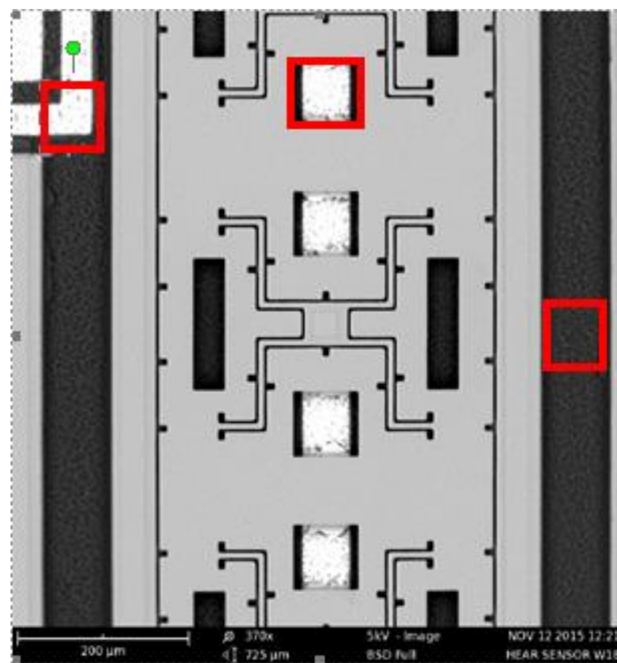

Figure 6-5 SEM image released elements that underwent thick Ti/Cu sputtering. Areas indicated by red squares show some places where grainy organic residue is evident

An unexpected potential failure mode was observed during SEM analysis of elements from a wafer that had undergone a thick Ti/Cu sputter for its sacrificial layer. Upon close inspection it was observed that the floating element had made contact with one of the electrodes causing the element to short (See figure 6.6). This may be caused during the release stages of the element where capiliary forces cause the shuttle to twist and touch one of the electrodes. These capiliary forces can be attributed to the wet etch, and rinses the elements must undergo prior to drying. Future work on studying this failure mode is discussed in chapter 7.2. Special attention will be spent on seeing if this occurs on most dies, since even if high quality metal films are achieved this type of failure mode may also be a primary cause of shorted elements.

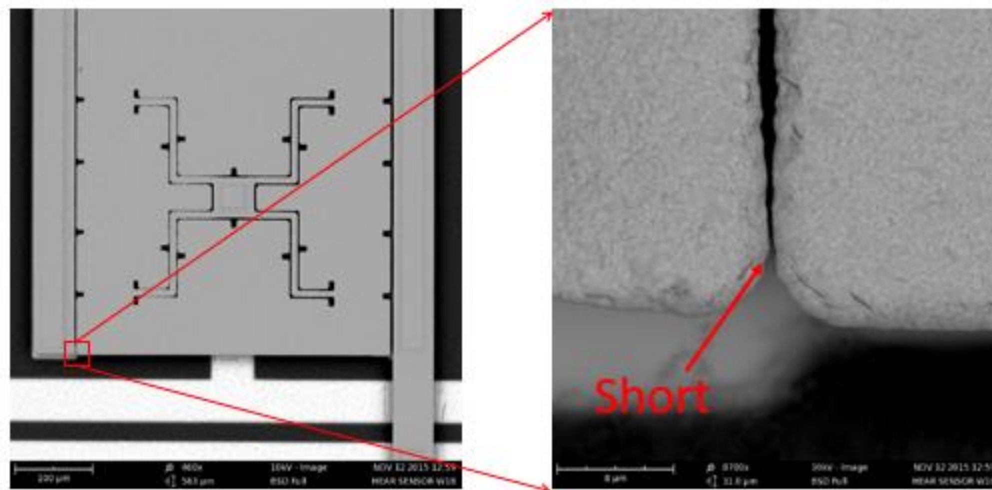

Figure 6-6 New observed failure mode during SEM image capturing of MEMS shear sensor elements. Here the floating element is shown to be touching one of the fixed electrodes causing the element to short.

6.3 Cr/Au and Ti/Cu Evaporation at Harvard CNS

Results from the thick Ti/Cu sputter led the group to believe that the NSC3000 sputter tool would be insufficient to produce high quality clean films. The sputter tool is shared by other groups at Tufts University that use various materials. In addition, the base pressure in the tool is very poor, never better than 10^{-4} Torr. In some cases these materials are organic which after inspection of some shear sensor elements led the group to believe that Cr/Au films and Ti/Cu films sputtered in the NSC3000 could contain some

unwanted contaminants. This could explain why delamination occurred previously in sputtered Cr/Au films and why grainy residue was observed in Ti/Cu films.

Further investigation of the sputter tool also showed that base pressure and process pressure readings from the NSC3000 may be inaccurate. After replacing a pressure gauge in the tool it was observed that pressure increased by a significant amount. Previously base pressure readings had shown to be in the 10^{-7} Torr range; after the change this reading increased to the 10^{-4} Torr range. It was concluded that previous pressure readings may have not been what the group had thought it to be. Such poor base pressure is another cause for low quality films achieved from the tool since low base pressure is needed to purge the chamber of contaminants from atmosphere.

In order to pursue higher quality Cr/Au and Ti/Cu films it was decided that these shear sensor wafers should have metal layers outsourced to a cleaner tool; one that has restrictions on what type of materials are used in it. Currently, the closest source to such a tool has been at Harvard CNS, where the clean room facility is home to a few evaporation tools. Due to this switch a few process parameters have been changed. Currently the Cr/Au process involves a base pressure of <1e-6 Torr, Cr thickness of 15 nm, Au thickness of 150 nm, a Cr deposition rate of 2 A/s, and a Au deposition rate of 2 A/s. The increase in Cr/Au thickness has been implemented to increase the conductivity of electrode connections, and it is possible since delamination is less of a concern in the evaporation process. The Ti/Cu process involves a base pressure of <1e-6 Torr, Ti thickness of 30 nm, Cu thickness of 300 nm, a Ti deposition rate of 1.1 A/s, and a Cu deposition rate of 3.0 A/s. From the switch the films were observed to be of higher quality, as a result it was not necessary to attempt a long Ti/Cu deposition in order to skip Cu plating steps.

An Image of the shear sensor after a Cr/Au evaporation deposition can be seen in figure 6.7, and an Image of the shear sensor after a Ti/Cu evaporation deposition can be seen in figure 6.8. Some downsides of the process is that each deposition at Harvard is costly, and having to transport wafers to and from different clean rooms can delay the micromachining process.

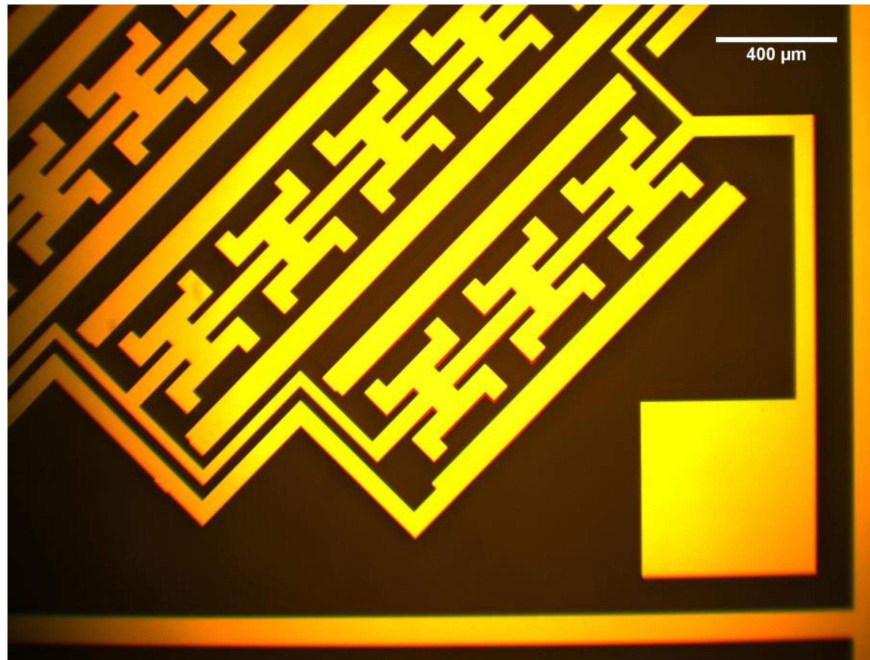

Figure 6-7 Image of MEMS shear sensor wafer after Cr/Au (15 nm / 150 nm) Evaporation from Harvard CNS.

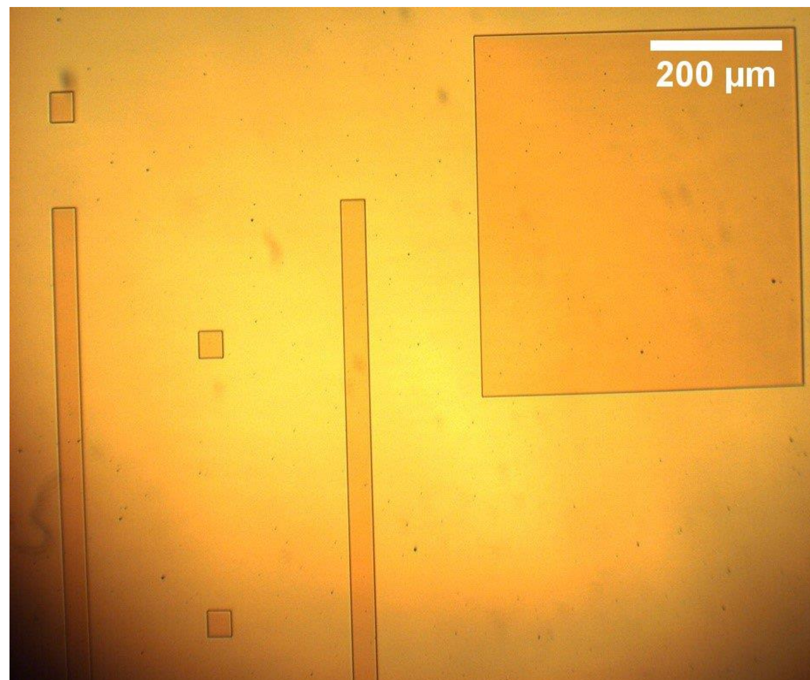

Figure 6-8 Image of MEMS shear sensor wafer after Ti/Cu (30 nm / 300 nm) evaporation from Harvard CNS.

Most recent results from this change has resulted in working chips. Using the same parameters used in measuring device capacitance from thick sputtered Ti/Cu chips

(1 kHz signal through the probes, driving that signal at 1 Volt, with a zero DC bias), four chips exhibited high resistance and reasonable capacitance values. Data on these chips can be seen in table 6-2.

Table 6-2 Resistance and Capacitance data on released MEMS Shear Sensors. These sensors underwent Cr/Au and Ti/Cu evaporation, 5 µm plated Ti/Cu sacrificial layer, >1 week etch, and CPD drying. Many groups experienced high resistance leading to the conclusion that these elements aren't stuck down.

Chip 16			
Top/Bot Electrode	Group	Resistance	Device With Stray Cable Capacitance Subtracted Out
Bot	A	30.7 Ω	
Top	A	25.4 Ω	
Bot	B	2.3 GΩ	5.02 pF
Top	B	2.3 GΩ	5.06 pF
Bot	C	46.2 Ω	
Top	C	42.6 Ω	
Top	D	2.3 GΩ	5.05 pF
Bot	D	2.5 GΩ	4.79 pF
Chip 17			
Bot	A	1.2 GΩ	9.40 pF
Top	A	550 MΩ	9.41 pF
Bot	B	27.1 Ω	
Top	B	2.2 GΩ	5.27 pF
Bot	C	1.4 GΩ	8.92 pF
Top	C	1.26 GΩ	9.89 pF
Top	D	2.4 GΩ	4.93 pF
Bot	D	2.2 GΩ	4.84 pF
Chip 18			
Bot	A	29.0 Ω	
Top	A	25.7 Ω	
Bot	B	2.2 GΩ	4.75 pF
Top	B	2.4 GΩ	4.67 pF
Bot	C	33.0 Ω	
Top	C	49.3 Ω	
Top	D	2.4 GΩ	4.36 pF
Bot	D	2.3 GΩ	4.70 pF
Chip 19			
Bot	A	1.4 GΩ	9.20 pF
Top	A	1.3 GΩ	8.78 pF
Bot	B	2.3 GΩ	5.26 pF
Top	B	2.3 GΩ	4.85 pF
Bot	C	1.3 GΩ	9.26 pF
Top	C	37 MΩ	9.25 pF
Top	D	44.3 Ω	
Bot	D	2.3 GΩ	7.75 pF

All four chips have at least two working capacitors making them good candidates for flow testing. An interesting thing to note is that when these chips were first

connected for measurements resistance seemed to be drifting and unstable. From SEM images of devices that have undergone Cr/Au and Ti/Cu evaporation, 5 μm plated Ti/Cu sacrificial layer, >1 week etch, and CPD drying, it was found that underneath the floating element stalactites exist; this is most likely due to roughness observed in Copper plated films. Introducing brighteners in the Copper solution in future fabrication runs may help to alleviate high roughness and decrease the amount of stalactites formed. SEM images of chips that have underwent this updated fabrication process can be seen in figures 6.9, 6.10, and 6.11.

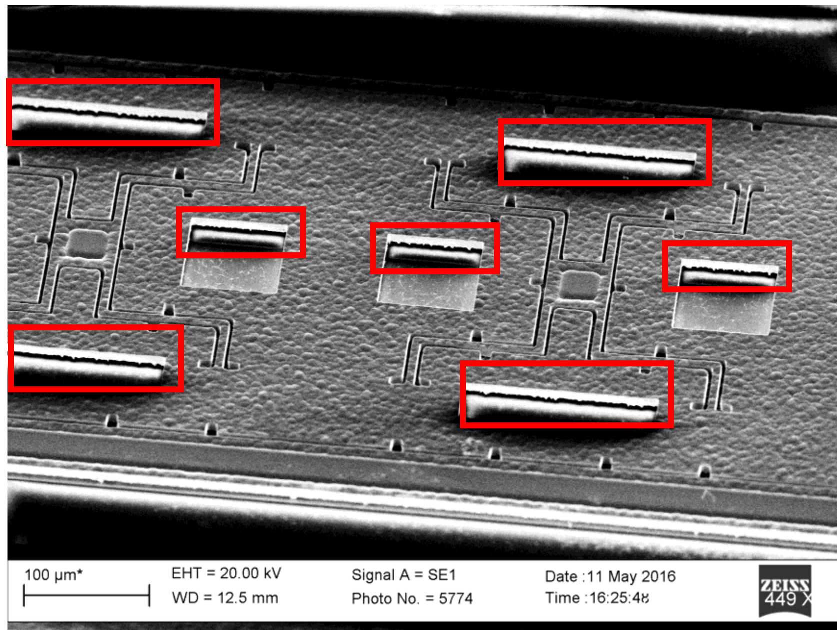

Figure 6-9 SEM image of two shear sensor elements that have undergone Cr/Au and Ti/Cu evaporation at Harvard CNS. Areas in red indicate the appearance of stalactites.

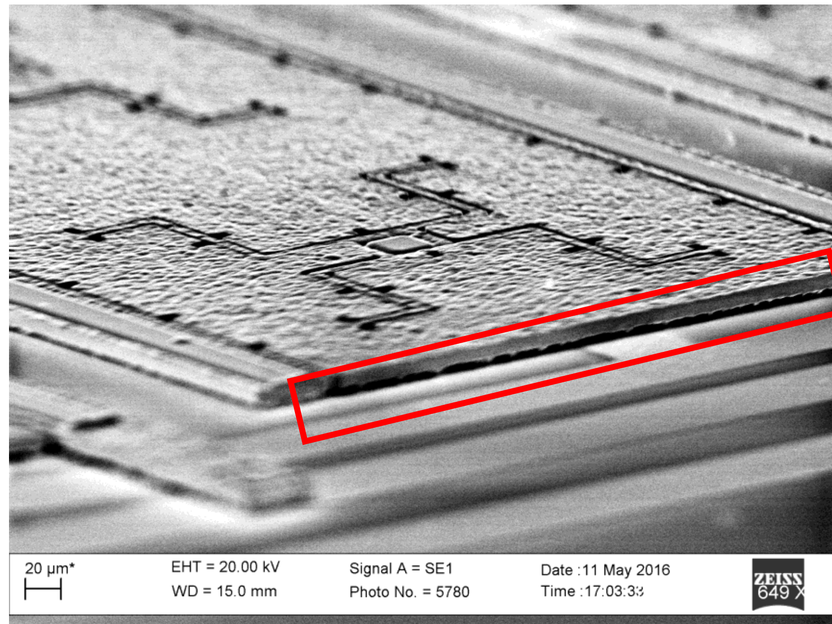

Figure 6-10 Close up SEM image of a MEMS floating element from the same chip in figure 6-2. Areas in red indicate the appearance of stalactites.

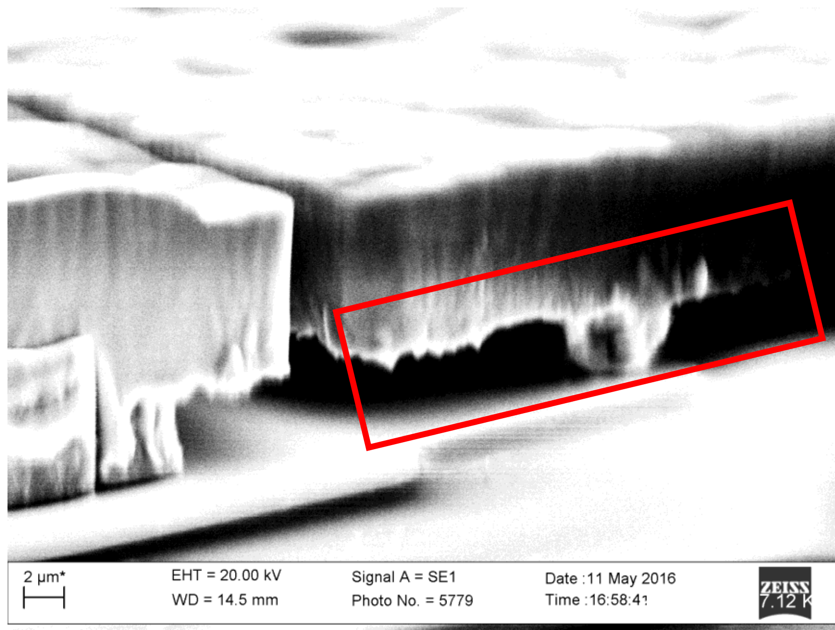

Figure 6-11 Close up SEM image of MEMS shear sensor from the same chip as in figures 6-2 and 6-3. Areas in red indicate the appearance of stalactites that are potentially the cause of shorted elements.

To fix the drifting problem a 10 V dc bias across the capacitor was applied which resulted in an increase of resistance up to the GΩ range and a settled out capacitance

value. It is predicted that a high bias is potentially capable of blasting away unwanted stalactites, fixing the short, and knocking the floating element loose. This 10 V DC bias was applied to 50-70% of the working elements in order to get good capacitance and resistance measurements. Doing this also made measurements more repeatable. More research, and additional capacitance testing must be done in order to make further conclusions about stalactites and drifting values in these devices.

From the data and table 6.2 it is observed that the measured capacitance of groups A and C (9-9.5 pF) is double the capacitance of groups B and D (4.5-5 pF). This is consistent with modeling predictions since groups B and D have half the number of elements; hence should have half the magnitude of capacitance compared to groups A and C. Another thing to observe is that actual capacitance measurements are slightly higher than expected (modeling results suggest capacitance should be around 2 pF).

Further experiments have been carried out on Chip 19 from this updated fabrication process. The chip's response to electrostatic drive was measured using a Laser Doppler Vibrometer. Group B was driven using a 9 Volt DC + 1 Volt Parallel sine wave, and its LDV response was gathered using a velocity decoder with filtering turned off (1.5 MHz bandwidth). Four collected swept sine results were gathered (1. Corner next to the driven electrode, 2. Corner opposite to the driven electrode, 3. At the Middle of the element, 4. On a pad off of the element). Results can be seen in figure 6.12.

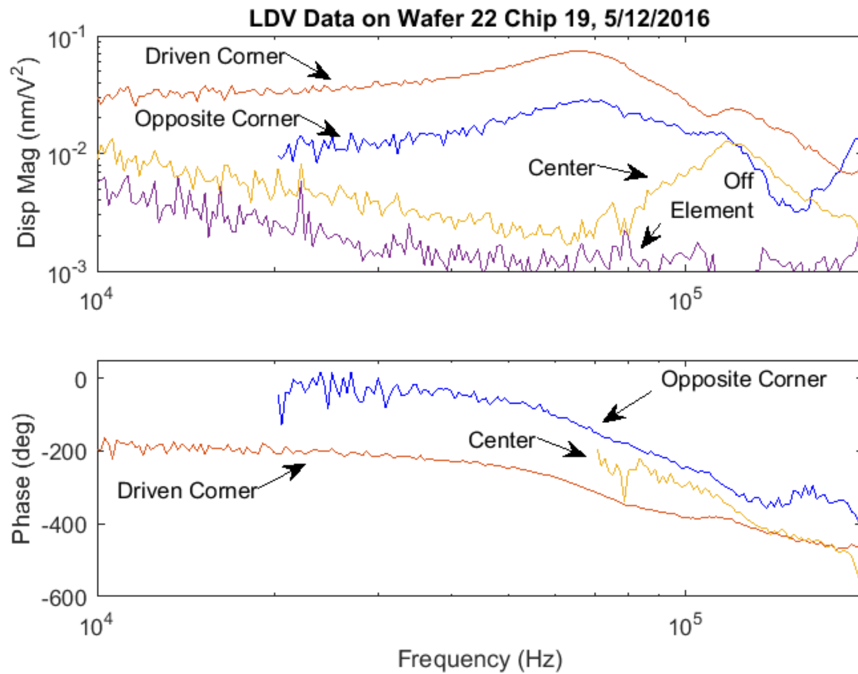

Figure 6-12 LDV data on chip 19.

Results suggest that there is more motion at the corner near the drive, less motion on the opposite corner, the least motion in the center, and no motion on the connection pad; all results suggesting reasonable motion of the sensor. Based on the levels of vibration and phase it was also gathered that there exists a rocking mode around 66 kHz and a bouncing mode around 120 kHz. Compared to modeling results these frequencies are higher than expected (modeling predictions suggested a rocking mode frequency of 19.5 kHz and a bouncing mode frequency of 25.2 kHz). Modeling predictions were gathered with the assumption that the element was in vacuum, whereas LDV measurements have the additional influence in air which is enough to shift modal frequencies of the device. More research needs to be done to gather more information on discrepancies between actual results and modeling results.

6.4 Results from RF SiO_2 Sputter

Figure 6-13 Image of MEMS shear sensor wafer after RF SiO_2 Sputtering.

RF sputtering of SiO_2 was attempted after the pattering, deposition, and lift off of Cr/Au evaporated films. Delamination and contamination was not a concern in this sputtering process since SiO_2 sputtering is possible at the Tufts Micro and Nano Fabrication Lab from a new Angstrom NexDep tool. This tool has many restrictions on what materials are allowed, and for the purpose of these experiments only shear sensor wafers have been processed in this tool. After deposition the SiO_2 the films seemed high quality enough to continue through the process (See Figure 6.13). After attempting lithography on top of this layer it was observed that the surface of the SiO_2 showed signs of cracking. An image of this cracking phenomenon can be seen in figure 6.14. Cracking is attributed to temperature changes in the SiO_2 film post RF deposition, and more work is to be done to optimize the process (See Chapter 7.2).

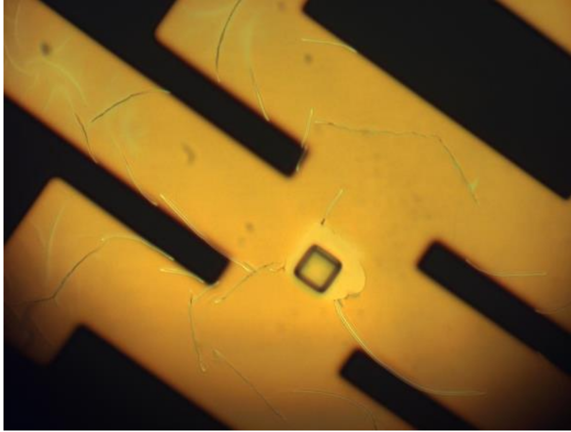

Figure 6-14 Cracking observed in RF sputtered SiO_2 after attempting to perform lithography.

7 Conclusion and Future Work

Aside from learning how to surface micro machine devices, operate tools, and adjust to a clean room environment, one of the key things I have learned from this experience is how difficult it may sometimes be to keep a process controlled in a college lab environment; an environment that does not have the luxury of isolating tools and space to solely one process. Since the start of the summer most work on this new generation MEMS shear sensor has been focused on improving the microfabrication process in order to yield enough devices for testing. Improving yield has been the largest road block, one that has required revising the process multiple times and processing multiple wafers under different conditions.

Revising a process typically involves isolating potential problem steps; steps in the process that are the most likely to cause stiction or delamination of films. It is often a risk to change a few parameters, test the new set up, and then attempt an optimized process on a process wafer. Changes can cause the loss of time and money; but in every case something new is learned about the surface micromachining process that leads the group closer to a final working optimized process. This chapter will summarize some of the key differences from the current generation of shear sensors compared to the older generation, modeling results, fabrication results, and highlight that changes in the fabrication process have resulted in four working chips.

7.1 *Hardware*

Each new generation MEMS floating element shear stress sensor at the Tufts Micro and Nano Fabrication lab is designed to fit on a 1 x 1 *cm* chip. The array layout of the device consists of four groups, each dedicated to both measure pressure gradient and shear stress sensitivity in one of two directions or in both directions. Each group may be isolated separately during measurements. Key element differences from a previous design by Zhengxin and Professor Robert White include the removal of surface topology, a change from comb fingers to parallel plates for differential capacitance measurements, and changes in beam structure in the shuttle.

The current surface micromachining process consists of 4 metal layers which includes copper and nickel electroplating; this follows the same structure as in the previous shear sensor design. Fabrication is conducted on a glass substrate. The most up to date process begins with a Cr/Au electrical interconnect layer that involves evaporating 15 nm of Cr and 150 nm of Au at Harvard CNS. This change was made after exploring the effects of process pressure and thickness of Cr/Au on the quality and stress on metal films. Evaporation provides us currently with the least contaminated layers since the NSC3000 is often shared with other users that fabricate with organic substances and has recently shown to produce undesirable base pressure. Evaporation currently provides us with lower film stress than sputtering.

The electrical interconnect layer is followed by the evaporation of 30 nm/ 300 nm of Ti/Cu. Evaporation is used here at Harvard CNS for similar reasons as the interconnect layer. Ti/Cu deposition is followed by copper plating in a homemade copper solution to complete the 5 µm thick sacrificial layer, which is then followed by Nickel plating a 10 µm thick structural layer. Other current fabrication changes include drying using a CPD rather than having released devices air dried in a low humidity environment. These changes have resulted in four working devices that will be packaged and tested in a flow cell in order to gather more information on device performance. These results will be used to make comparisons to quasistatic modeling discussed in previous chapters.

7.2 *Modeling*

From structural, electrostatic, and fluids models of this MEMS shear sensor it was found that pressure gradient sensitivity is decreased and shear stress sensitivity is increased compared to the previous generation of MEMS shear sensor. This is based on two key assumptions: one being that response of the element is due to pure shear on only the top surface of the element, and that all additional response aside from shear is due to a pressure gradient. These assumptions have built up these models that are discussed in chapter 2. For groups A and C pressure gradient sensitivity is taken to be -0.6 aF/(Pa/mm) while shear stress sensitivity is 0.15 fF/Pa. For groups B and D pressure gradient sensitivity is -0.3 aF/ (Pa/mm), while shear stress sensitivity is 0.074 fF/Pa. Once these devices can be tested it is possible to check how well model results compare

with actual results. From those comparisons assumptions may be clarified and new conclusions may be made.

7.3 *Future Work*

There are different areas of improvement in the micromachining process that can be explored in future work that aims at further improving yield of these MEMS shear sensors. Main goals for this new generation of shear sensors involves having low stress and high quality metal films to reduce stiction of elements. Future work also includes the packaging and testing of four working chips that were discussed in chapter 6.

7.3.1 Fabrication

The following sections include recommendations to the surface micromachining process. Some of these suggestions will help decrease stiction, are worth looking into as other alternatives to the process, or is useful for improving setup for a particular step in the process. Tufts Micro and Nano Fabrication lab is capable of many different processing techniques which are worth exploring to increase the range of possible fabrication options for this particular device.

7.3.1.1 Electroless Nickel

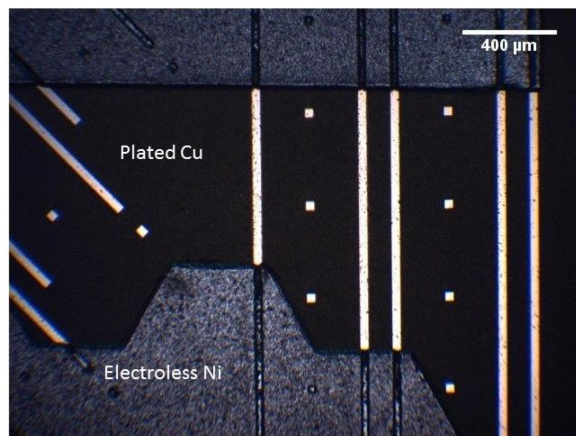

Figure 7-1 Patterned electroless plated Nickel on patterned plated Copper.

Electroless Nickel is an alternative to Nickel electroplating during the construction of the structural layer of the shear sensor. Experiments led by Kevin Ligonde have shown that the use of commercial electroless Nickel plating solution, MCT-14, is capable of plating Nickel on Copper. Prior to plating it is suggested to place

the substrate in MCR-14/Activator for two minutes. The activator slightly etches the copper surface to make the surface more adhesive for the Nickel. Plating typically involves a solution temperature of 80ºC and stirring agitation for a solution in a petri dish. Results have shown to produce a plating rate of 300 nm/min. One key advantage to electroless Nickel plating is that it requires a less intensive setup then electroplating Nickel since the need for a cathode and anode is eliminated. It is possible to plate hard baked AZ9260 although more work should be done to optimize lithography parameters prior to plating, or optimize electroplating parameters to avoid delamination of Nickel film on photoresist for thicker plated Nickel. Figure 7.1 shows patterned plated Nickel through this process on top of patterned plated Copper.

7.3.1.2 Introduction of New Equipment

The Tufts Micro and Nano Fabrication Lab is expecting to have a Denton Vacuum E-Beam Evaporator online in the upcoming months. This will provide the lab with an alternative to sputtering for the deposition of metal films. With the introduction of this new equipment it is likely that it will be limited to only a few materials to reduce the chances of contamination. The lab is also expecting the revamping of the NSC3000 sputter tool due to the discovery of poor resulting base pressure. Having both an evaporator and upgraded sputter tool will reduce the need to make depositions at Harvard and keep processing at TMNF.

7.3.1.3 SAM

Another method for reducing stiction is introducing the surface of the device, after release but prior to drying, with a Self Assembled Monolayer (SAM). The most common SAM coating is octadecyltrichlorosilane, and it is used to reduce surface energies during drying [12]. Since the structure of these elements is made up of Nickel a different SAM coating is needed, namely n-Dodecanethiol [13]. If stiction continues to be a problem, even after having metal layers deposited at Harvard or in new tools at TMNF, SAM could be a useful tool. It will, however, require time to adapt into the current surface micromachining process and involve the removal of surface oxides prior to SAM coating using Hydrogen Chloride (HCl) or Ammonium Hydroxide (NH4OH) [13].

7.3.1.4 SiO_2 Optimization

After observing cracks in RF SiO_2 sputtering it was found that more research and work can be done to optimize the process. Other work on RF SiO_2 suggests that cracking may be due to the porosity of RF SiO_2 films during higher power deposition. When SiO_2 films were exposed to the environment post sputtering cracking was also observed. Cracking did not occur immediately but instead over some time which is how cracking was observed at TMNF [14, 15]. This work speculated that due to the porosity of the film, SiO_2 is susceptible to trapping moisture when removed from a vacuum environment. This causes high residual stresses in the film that may lead to cracking [14, 15]. Another cause of high stress in SiO_2 film may be due to large temperature changes; in Chandra and Wu's work experiments that ran depositions with a heated substrate (90ºC) and were then followed by exposing the film to room temperature also caused cracking [14, 15].

RF sputtered SiO_2 with the lowest stress were observed in films that introduced O_2 during deposition, and at higher O_2 concentration during sputtering, films were observed to have smaller less porous grain sizes [15, 16]. If SiO_2 films are to be deposited or grown at TMNF work will have to be done on the following:

- Lower powered RF deposition (one disadvantage are lower power results in lower deposition rates).
- Substrate heating and effects of temperature changes on film.
- Introduction of O_2 during sputtering (possible in the Angstrom NexDep).
- Longer, 15-20 minute, target clean to remove any contaminates on the SiO_2 target.
- Post-annealing practice for thermally grown SiO_2 films, however, requires a source of Silicon.

References

[1] D. H. Tao Pan, Mchran Mchregany, Eli Reshotko, Steven Gaverick, "Microfabricated Shear Stress Sensor " *AIAA Journal,* vol. 37, 1999.

[2] Z. Zhao, M. Shin, J. M. Gallman, and R. D. White, "A Microfabricated Shear Sensor Array on a Chip With Pressure Gradient Calibration," *Sensors and Actuators A: Physical,* vol. Volume 205, pp. 133-142, January 1 2014 2014.

[3] J. W. Naughton and M. Sheplak, "Modern Developments in Shear-Stress Measurement," *Progress in Aerospace Sciences,* vol. 38, pp. 515-570, 8// 2002.

[4] R. T. H. Martin A. Schmidt, Stephen D. Senturia, Joseph H. Haritonidis, "Design and Calibration of a Microfabricated Floating-Element Shear-Stress Sensor," *Transactions of electron Devices,* vol. 35, pp. 750-757, 1988.

[5] A. F. J. Luo, S. Spearing, N. Fleck and W. Milne, "Young's Modulus of Electroplated Ni Thin Film for MEMS Applications," *Mater Lett,* vol. 58, pp. 2306-2309, 2004.

[6] J. R. Davis, "ASM Specialty Handbook - Nickel, Cobalt, and Their Alloys," ASM International," p. 4, 2000.

[7] J. W. Hutchinson, M. D. Thouless, and E. G. Liniger, "Growth and Configurational Stability of Circular, Buckling-Driven Film Delaminations," *Acta. Metall. Mater.,* vol. 40, pp. 295-308, June 11 1991 1992.

[8] C. W. Tan and J. Miao, "Optimization of Sputtered Cr/Au Thin Film for Diaphragm-Based MEMS Applications," *Thin Solid Films,* pp. 4921-4925, March 24th 2009 2009.

[9] G. C. A. M. Janssen, M. M. Abdalla, F. V. Keulen, B. R. Pujada, and B. V. Venrooy, "Celebrating the 100th Anniversary of the Stoney Equation for Film Stress: Develpoments from Polycrystalline Steel Strips to Single Crystal Sillicon Wafers," *Thin Solid Films,* vol. 603, 2008.

[10] M. Zecchino, "Thin Film Stress Measurement Using Dektak Stylus Profilers," B. Veeco Instruments Inc, Ed., ed. Bruker.

[11] Industrial Glass Technologies, "Sode-Lime-Silica Float Glass Selected Properties," ed. Industrialglasstech.com.

[12] M. R. H. Uthara Srinivasan, Roger T. Howe, Fellow, IEEE, Roya Maboudian, "Alkyltrichlorosilane-Based Self-Assembled Monolayer Films for Stiction Reduction in Silicon Micromachines," *Journal of Microelectromechanical Systems,* vol. 7, pp. 252-260, 1998.

[13] Z. Mekhalif, J. Riga, J. J. Pireaux, and J. Delhalle, "Self-Assembled Monolayers of n-Dodecanethiol on Electrochemically Modified Polycrystalline Nickel Surfaces," *Langmuir,* vol. 13, pp. 2285-2290, 1997/04/01 1997.

[14] V. B. a. S. Chandra, "Silicon Dioxide Films by RF Sputtering for Microelectronic and MEMS Applications," *Journal of Micromechanics and Microengineering,* 2007.

[15] W.-F. Wu and B.-S. Chiou, "Properties of radio frequency magnetron sputtered silicon dioxide films," *Applied Surface Science,* vol. 99, pp. 237-243, 7/1/ 1996.

[16] E. F. H.U Schreiber, "High Quality RF-Sputtered Silicon Dioxide Layers."*Journal of Electrochemical Society.* 1976.

Appendix A Alignment Slide Mask

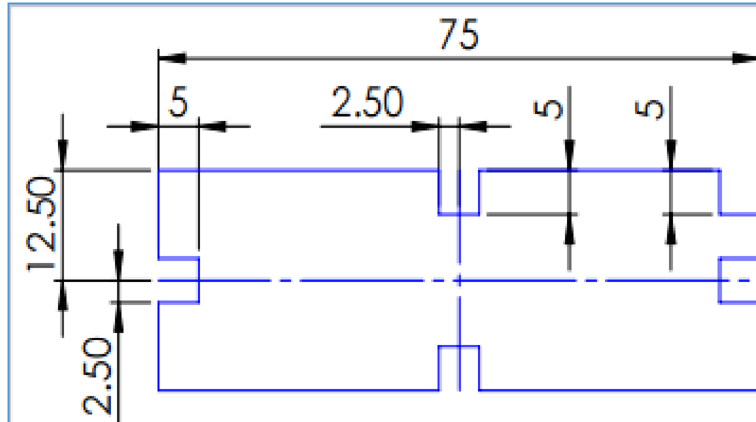

Appendix B Surface Micromachining Runsheet

RUNSHEET

Process Name: Nickel Surface Micromachining
Process Goal: Shear sensor run with glass substrate, Nickel structural layer 10 μm thick, Cu sacrificial layer 5 μm thick, and Cr/Au interconnect.
With Evaporated Cr/Au and Ti/Cu at Harvard
Author: Daniela Torres, Robert White, Jim Vlahakis, Zhengxin Zhao
Revision Date: February 19, 2016

Refer to SOPs: "Standard Lithography", "OAI Aligner", "Laurell Spinner", "NSC-3000 Sputter", "March RIE", "Copper Electroplating", "Nickel Electroplating", "LOR Liftoff".

Starting Substrates: 100±.2mm Soda Lime 550±50μm Thick DSP (60/40) W/Rounded Edges & Primary Flat Only.

Step Name	Parameters	Measurements/ Comments	Date Complete
1. Piranha Clean (REQUIRED – important for good results in #3)	Piranha clean starting substrates, 1:1 H_2SO_4:H_2O_2 (30%) by volume. 10 mins clean, 3 mins DI water x 2.		
2. O_2 Clean (REQUIRED)	200W, 120sec, 100% O_2 (~300 mT) in March RIE		
3. Lithography #1	LOR20B: 500 rpm 4sec, 2000 rpm 45sec, 200C 5min softbake	LOR20B: 2000 rpm = 2.0 μm	

Metal Mask v4	(dirty hotplate ***no tinfoil*,** with glass cover); AZ9260: 500 rpm 8 sec spread, 6000 rpm 60 sec spin, 115C 2 min softbake (clean hotplate with tinfoil), 30 sec exposure (hard contact), 2 min 20 sec develop in AZ400K:water 1:3, 2 x 2 DI water rinse, air gun dry	AZ9260: 6000 rpm = ___ µm	
4. O_2 Descum	200W, 60 sec, 100% O_2 (280 mT) plasma descum in March RIE	Etch rate ~ 0.4 µm/min	

5. Sputter Cr/Au	15 nm Cr/150 nm Au evaporated in EE4 ebeam evaporator at Harvard	Base pressure: Ti dep rate: Cu dep rate:	
6. Liftoff	Heated Remover 1165 in glass petri dish (covered) at 60C (80C hotplate temp) for > 3 hr. Transfer to fresh Remover, sonicate 5 minutes, DI water rinse 1000 mL beaker 3 mins x 2. Blow dry.	Measure thickness. Center: _____ nm Edge: ______ nm	
7. Lithography #2 "Anchor Liftoff" Mask v4 **IMPORTANT NOTE: This is mask #4 … when doing alignment it aligns to alignment mark #4!!!! (shear sensors)**	LOR20B: 500 rpm 4sec, 2000 rpm 45sec, 200C 5min softbake (dirty hotplate *no tinfoil*, with glass cover); AZ9260: 500 rpm 8 sec spread, 6000 rpm 60 sec spin, 115C 2 min softbake (clean hotplate with tinfoil), 30 sec exposure (hard contact), 2 min 20 sec develop in AZ400K:water 1:3, 2 x 2 DI water rinse, air gun dry	LOR20B: 2000 rpm = 2.0 µm AZ9260: 6000 rpm = ___ µm	
8. O_2 Descum	200 W, 60 sec, 100% O_2 (280 mT) plasma descum in March RIE		

9. Ti/Cu Evaporation	30 nm Ti/300 nm Cu evaporated in EE3 ebeam evaporator at Harvard	Base pressure: Ti dep rate: Cu dep rate:	
10. Liftoff	Heated Remover 1165 in glass petri dish (covered) at 60C (80C hotplate temp) for > 3 hr. Transfer to fresh Remover, sonicate 5 minutes, DI water rinse 1000 mL beaker 3 mins x 2. Blow dry.	Measure thickness. Center: _____ nm Edge: ______ nm	

11. Lithography #3 "Anchor Plate" Mask v3 (shear sensor) **IMPORTANT NOTE: This is mask #2 … when doing alignment it aligns to alignment mark #2.**	HMDS/AZ9260 500 rpm 8 sec spread, 3000 rpm 60 sec spin, 120C 3 min softbake, 35 sec exposure (hard contact), 5 min develop in AZ400K:water 1:3, 2 x DI water rinse, air gun dry	Measure resist thickness: __________ μm (expect 6 μm)	
12. O_2 Descum	200 W, 60 sec, 100% O_2 (280 mT) plasma descum in March RIE		
13. Copper Electroplating	Plate on thick Cu (filter). See Cu plating SOP. 0.8M $CuSO_4$, 1.5M H_2SO_4, 80 ppm Cl^-, 20^oC, 5 mA/cm^2 results in ~130 nm/min. 2 x DI water rinse. Wafer area 78 cm^2. So 390 mA gives ~5mA/cm^2. Shear sensor: Plate for 30 minutes. Target total Cu thickness 5 μm. cMUT: Choose time for desired thickness (~130 nm/min). *Stop deposition after half the expected dep time. Measure Cu thickness, and adjust length of remaining time accordingly.*		

14. Strip Photoresist	5 minute acetone soak, 2 min IPA, 2 min x 2 water, air dry,		
15. O_2 Descum	200W, 120sec, 100% O_2 (300 mT) in March RIE		
16. Measure Cu	DekTak Cu thickness	Total Ti/Cu/CU thickness:	

17. Lithography #4 "Anchor Double Expose" Mask (shear sensor) **And** **"Structure v4" mask (shear sensor)**	HMDS/AZ9260 500 rpm 8 sec spread, 3000 rpm 60 sec spin, 120C 3 min softbake, 40 sec exposure (hard contact) "anchor double expose mask", 5 min develop in AZ400K:water 1:3, 2 x DI water rinse, air gun dry *Examine. If fully developed, continue. If not, develop a bit more, repeat until fully developed, then continue to second spin:* HMDS/AZ9260 500 rpm 8 sec spread, 3000 rpm 60 sec spin, 120C 3 min softbake, 30 sec exposure (hard contact) "anchor double expose mask", 3 min develop in AZ400K:water 1:3, 2 x DI water rinse, air gun dry Examine. Repeat additional develop steps 30 second incremements until fully developed.	Measure resist thickness: __________ μm (expect 12 μm)	

18. O_2 Descum	200W, 60 sec, 100% O_2 (280 mT) plasma descum in March RIE		

19. Copper oxide etch	Etch copper oxide off in 10 % by volume sulfuric acid in water, 30 second dip, then 1 minute DI water rinse, and immediately into nickel plating solution.		
20. Nickel Electroplating	Plate on thick Ni. See Ni plating SOP. NICKEL SULFAMATE SEMI BRIGHT RUT MECHANICAL AGITATION, 50C (hotplate front panel temp for large tank = 180 C), 5 mA/cm^2 results in 100 nm/min. Structure mask has an area of 32 cm^2 (does not include edges or edge rectangles for both shear sensor and cMUT). Use 160 mA to achieve 5 mA/cm^2. Target thickness 10 μm (100 mins) for shear sensor, 5 um (50 mins) for cMUT. May want to stop half way and measure on DekTak. Uniformity problems can exist – rotating 180° halfway through might be good.		
21. Strip Photoresist	10 minute acetone soak, 5 min IPA, DI water spin, spin dry.		
22. Measure Ni	DekTak Ni thickness at 5 points	Ni thickness: Flat (bottom): Center: Top: Left: Right:	
23. Protect wafer	Spin on HMDS/AZ9260 at 3000 rpm, softbake 120C, 4 mins.		
24. Dice wafer	MA dicing saw – dice into individual dies. Die size (center to center on cuts = 10.1 mm)		
25. Strip Photoresist	10 min acetone soak, 5 min IPA, 5 min x 2 water. Blow dry each chip carefully (place on towel, blow straight down)		
26. O_2 Clean	200W, 120 sec, 100% O_2 (280 mT) plasma clean in March RIE		

27. Copper Wet Etch (Release)	1:1:18 CH_3COOH: H_2O_2: Water 1 day, 10min x2 DI water rinse, IPA 10 min, Methanol 30 min,		
28. Dry	Option #1 : 2 hr dry in drybox at reduced relative humidity Option #2: Tousimis critical point drier.		